Chapter 1

INTRODUCTION

For much of the past decade, GaN has attracted much attention because of its specific material properties which are suitable for several important technological applications. The wide and direct bandgap make it suitable for blue and UV wavelength light–emitting diodes (LEDs), laser diodes and photo detectors. With shorter wavelength than the contemporary red laser diodes, a blue laser based photo-disk data storage system can store much more data. Since GaN-based materials have a wide band gap, a high breakdown electric field and a high saturation velocity found at high electric field (Fig.1), GaN-based electronic devices have also received much attention because they can operate at high microwave power and in a high temperature environment.

The wide bandgap (3.4eV) nature has two advantages: One is that it keeps GaN remains intrinsic at higher temperatures than GaAs (1.4eV) and Si (1.12eV). Therefore, GaN based electronic devices can operate at higher temperatures than contemporary electronic devices. As a result, the volume and cost of cooling systems could be reduced. The other is that the high breakdown field which is calculated to be 5MV/cm, much higher than Si (0.2MV/cm) and GaAs (0.4MV/cm) since breakdown field is roughly related to the square of energy gap. The high breakdown field character of material is essential for devices with high breakdown voltage.

The AlGaN/GaN heterostructure enables us to fabricate a high power and high frequency operation device called HEMT

(High-Electron-Mobility-Transistor). Wurtize AlN and GaN grown on sapphire have bandgaps of 6.2eV and 3.4eV. With moderate Al composition AlGaN compounds we can obtain a bandgap discontinuity at the AlGaN/GaN interface without lattice mismatch leading cracks. Higher Al composition makes a larger AlGaN bandgap but also suffers from larger AlGaN/GaN interface lattice mismatch and result in dislocations or even cracks. According to the band-diagram there will be a 2-dimensional quantum well exist at GaN layer near the AlGaN/GaN interface (Fig.2). If the AlGaN/GaN HEMT structure is the Ga-faced polarization structure, electrons may come from surface and dopants. And the electrons will be dragged to the quantum well called two-dimensional electron gas (2DEG) efficiently. The reason is the sum of spontaneous polarization for GaN and piezoelectric polarization which comes from the AlGaN/GaN lattice mismatch strain is about ten times than GaAs. The two-dimensional electron gas (2DEG) has high electron mobility ($1300cmV^{-1}S^{-1}$) and high carrier density ($1\sim2E10^{13}$). With such high carrier density and mobility, high power at high frequency could be obtainable. Such devices are capable of cell phone base station power amplifiers, phase-array radars, automobile electronic applications and other high power, high frequency and high temperature condition uses.

In 1993, Khan et al. demonstrated the first AlGaN/GaN modulation-doped field electron transistor (MODFET) with a Gm of 23mS/mm and 2DEG mobility of $563cmV^{-1}S^{-1}$ at RT. They also reported the first microwave results with f_t of 11GHz and f_{max} of 14GHz. With the improvement of material quality and strong polarization effect at the Ga-face layers, nowadays GaN HEMT devices show remarkable high

frequency and high power properties. In 2001, Mishra group exhibited AlGaN/GaN HEMTs with Gm of 230mS/mm, f_t of 25-30GHz, f_{max} of 60-100GHz, saturation current 950mA/mm and 60~80V gate-drain breakdown, and a power density of 9.8W/mm at 8GHz. [1] .Such high power performance at high frequency makes GaN suitable for high power microwave devices.

For the fabrication of AlGaN/GaN HEMTs, isolation process needs to be done first. Since GaN lacks stable oxides which could be applied for isolation. The conventional isolation method is mesa dry etch. High energy halide and Argon mixed plasma bombards the surface and etches off unwanted region for isolation. However, surface damage and unwanted vertical cliff at the mesa edge will occur. Wet etching isolation for GaN is also hard since GaN is chemical stable. Therefore, ion implantation isolation is applied for its planar isolation process. A planar process is also better for device process and package process integration.

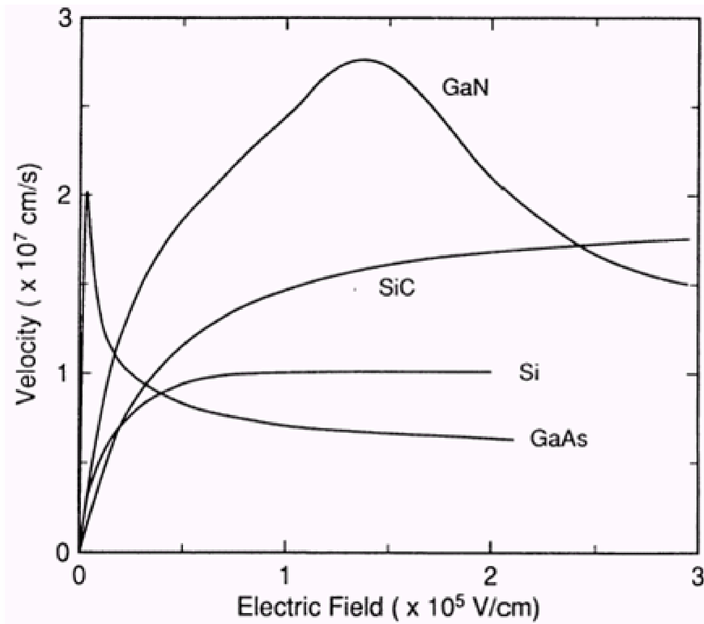

Electron drift velocity at 300 K in GaN, SiC, Si and GaAs computed using the Monte Carlo technique.

Fig.1 GaN exhibits high saturation velo city at high electric field

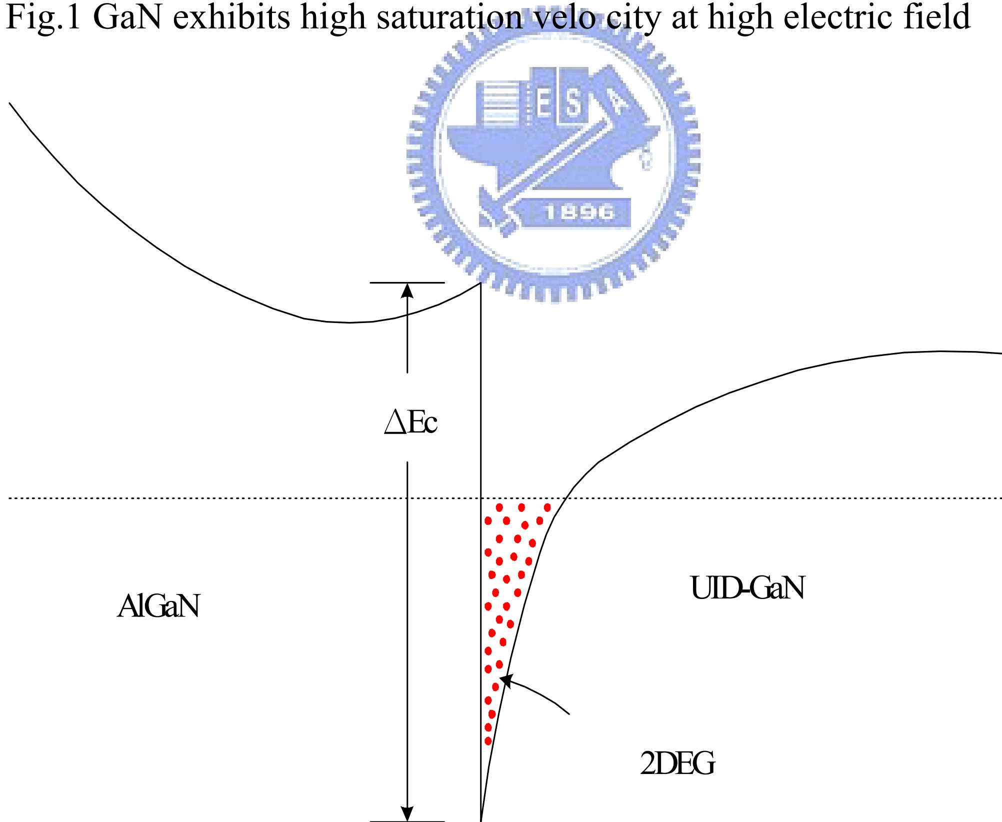

Fig.2 2DEG at AlGaN/GaN interface

Chapter 2

Ion Implantation Theory Background

2.1 Ion Implantation

Ion implantation is used for selective doping in the silicon industry for decades. First, PR mask was used to define the doping area and dopants with moderate dose and energy were implanted. After implantation, thermal annealing was applied for activation of dopants. In the early years of GaN people wanted to apply implant doping for GaN electronic devices. In 1995, a group used Ca and O for p and n type GaN, but they discovered the activation RTA temperature is above 1100°C. Only 3.6% O was activated after a 1050°C 30seconds RTA [2]. For the early studies of such implant doping and post annealing, they found that implantation will result in a highly resistive area. In 1995, another group used H, He and N for GaN implant isolation [3]. And the resistivity remained high even after post annealing for He and N implantation. As a result, ion implantation can be used for isolation of GaN.

Basically, ion implanted into a semiconductor undergoes collisions with the target atoms, and loss kinetic energy due to the ion stopping process. Much of the energy is transferred to the lattice which causes thermal spike or displacement and substitution of the target atoms. The lost of energy is determined by several factors, mainly electronic stopping and nuclear stopping. Electronic stopping means the implant ion is dragged by the electrons of the target. Nuclear stopping occurs as a result of elastic collisions between nuclei and implant ions, and transfer their energy to displace other nuclei, leading to a chain or cluster of

recoiled atoms. Nuclear stopping should play the most important role. According to basic modern physics, higher atomic mass atoms have larger collision cross-sections, which make them easier to collide. Thus with different implant ion mass will result in different implant depth and defect type. Besides ion mass, ion energy, implantation dose, implantation temperature and implantation angle will affect the implantation isolation effect physically. Ion species and post annealing procedure will affect the implantation isolation effect chemically. These will be discussed one by one in the later part.

First, we considered the physical ion impact induced defects by the category of ion mass, ion energy, ion dose, implant temperature and implant angle

I. Ion Mass:

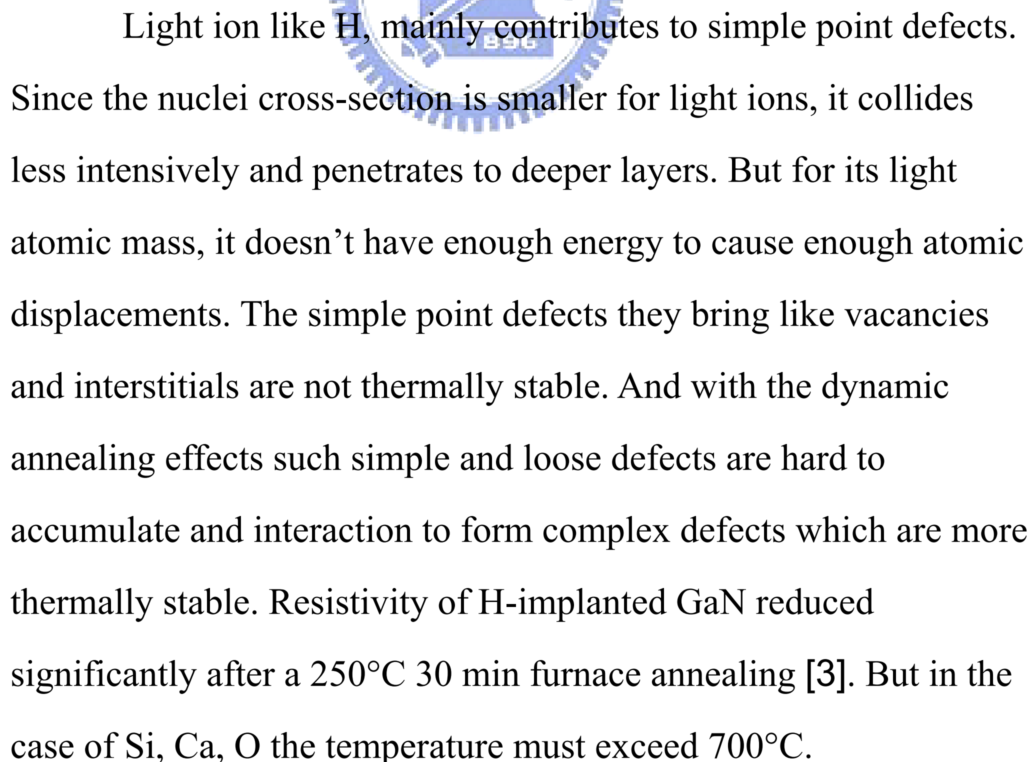

Light ion like H, mainly contributes to simple point defects. Since the nuclei cross-section is smaller for light ions, it collides less intensively and penetrates to deeper layers. But for its light atomic mass, it doesn’t have enough energy to cause enough atomic displacements. The simple point defects they bring like vacancies and interstitials are not thermally stable. And with the dynamic annealing effects such simple and loose defects are hard to accumulate and interaction to form complex defects which are more thermally stable. Resistivity of H-implanted GaN reduced significantly after a 250°C 30 min furnace annealing [3]. But in the case of Si, Ca, O the temperature must exceed 700°C.

Heavy ion like Au, will result in complex and intense defects and even amorphous if the damage level (and/or the energy

deposited in the collision cascade volume) exceed some threshold value. The high defect generation rate enhances the interaction of mobile defects and promotes the formation of complex defects rather than defect annihilation via dynamic annealing. But it needs a real good MeV scale implantor to have enough energy to implant Au to the desired depth. It also needs to take care for not implanting too much dose, or the lattice may transfer to amorphous after implantation. If amorphous does occur and then recrystallization takes place, currents may leak through grain boundaries since resistivity is smaller at that region

II. Ion energy:

TRIM is a helpful simulation program to calculate the ion and damage distribution by Monte Carlo method. Using this program we can calculate the moderate ion energy we need to cause damages at the desired depth. For the isolation of HEMT, we must have a damage peak at the 2-dimensional gas region since it is the conducting channel. We also need to have a damage distribution extend to enough depth, or the currents may flow under it. For such purpose, different ion mass and energies are applied for multi-implant to achieve best isolation effects. In Electronics Letters 1998, using P implant for shallow layer and He implant for deep layer with different energies was reported [4]. With the improvement of technology, ion implantor with much higher ion energy was used. Heavy ion like Au can be implanted with such high energy.

III. Ion dose:

For higher ion dose, more defects are formed. We should seek for a dose that is large enough to damage a large quantity of defects for isolation but not too large to result in an amorphourized layer. It is fortunately that GaN is extremely difficult to be amorphized by ion implant at RT when compared with Si or GaAs. Amorphous layers in Si and GaAs can be created by heavy ion implant at RT with dose of the order of $1*10^{14}cm^{-2}$, while GaN remain crystalline to the doses of at least $1.5*10^{15}$ cm^{-2} Au implant [5]. As a result, GaN is suitable for implantation isolation.

IV. Implantation temperature:

While implantation making defects in the lattice, a mechanism called dynamic annealing works simultaneously to recover the defects. For extra low temperature like LN_2 (liquid nitrogen), dynamic annealing is suppressed so the lattice is easier to be amorphous. On the other hand, implantation at higher temperature can suppress the accumulation of stable defects and amorphization as studied by Parikh et al. with RBS and XTEM [5]. For isolation purpose, RT implantation is more appropriate to cause accumulation of stable defects and avoid amorphization.

V. Implantation angle:

For epitaxy of wurtize GaN, we often grow GaN on a sapphire along the (0001) direction or you may say the c-axis. It is reported in 2003 that defect density is significantly reduced when implanting along the GaN c-axis and gradually increase when changing the implantation angle towards random implantation (i.e. 10 degree off the c-axis) [6]. A rather large 6.5 degree critical angle

is found for Er implanted GaN. If implantation is conducted within the critical angle, channeling effect will take place. Ions implanted toward the channeling direction will experience fewer collisions with lattice atoms and cause less damage. For isolation purpose we should alter the implantation angle to exceed the critical angle therefore to get enough defects.

2.2 Implantation Isolation

The implantation process can compensate a semiconductor layer either by damage or chemical mechanism. For damage compensation, the resistance typically goes through a maximum with increasing post-implantation annealing temperature as the damage is annealed out and hopping conduction is reduced. At higher temperatures the defect density is further reduced below which is required to compensate the material and resistivity decreases. For chemical compensation, the post-implantation resistance again increases with annealing temperature with a reduction in hopping conduction but it then stabilizes at higher temperatures as a thermally stable compensating deep level is formed. Typically there is a minimum dose (dependent on the doping level of the sample) required for the chemically active isolation species to achieve thermally stable compensation .The threshold dose increases linearly with the concentration of free carriers. It has a formula of $n(D) = n(0) – AD$, where D is the ion dose, n(D) is free carrier concentration in the conductive layer after implantation to dose D, and A is a constant which depends on ion mass and energy. Thermally stable implant isolation has been reported for n- and p-type AlGaAs where an Al-O complex is thought to form [7][8] and for C-doped GaAs and AlGaAs where a C-N

complex is postulated . [5] The defect levels estimated from Arrhenius plots of the resistance/temperature product are 0.83 eV for initially n-type and 0.90 eV for initially p-type GaN in Fig.1 [9]. These levels are still not at midgap, but are sufficiently deep to realize a sheet resistance $>10^9\,\Omega$/square. The implantation has also been reported to effectively isolate n-type GaN, with the material remaining compensated to over 850°C. For isolation of GaN, damage dominates rather than chemical compensation.

2.3 Material Analysis

We applied material analysis correlate isolation quality with material microstructure. TEM was applied for defect type and distribution while ESCA was applied for chemical bonding condition. AFM was used for surface morphology. The basic understanding of TEM and ESCA are described as follows.

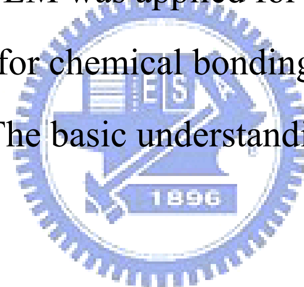
1896

2.3.1 TEM

TEM is one of the most powerful tool for material analysis. Knoll and Ruska (1932) developed the idea of electron lenses and Ruska received Nobel Prize in 1986. The transmission electron microscope is an analytical tool that allows detailed micro-structural examination through high-resolution and high-magnification imaging. It also enables the investigation of crystal structures, orientations and chemical compositions in phases, precipitates and contaminants through diffraction pattern, x-ray, and electron-energy analysis. Today's HRTEM can achieve magnifications of up to 500,000x and detail resolution below 1 nm. Quantitative and qualitative elemental analysis can be provided from

features smaller than 30 nm. For crystals with interplanar spacing greater than 0.12 nm, crystal structure, symmetry and orientation can be determined. A TEM is able to image the atomic arrangement of a single crystal and to identify the Burgers vector for a dislocation. Structural examination of defects, including stacking faults, interstitial, precipitates and vacancies is possible. But sample preparing is always a difficult and time consuming process. Since the electron beam must trans- through the specimen and remain bright enough to get image, the specimen must be thinned to less than 100nm, and even less than 50nm for high resolution. The common way of specimen preparing is to polish it to a certain thickness and then ion milling. Ion milling may cause two problems: one is ion damage of the specimen and the other is heating. So we must take care in all steps.

In our experiment, we use XTEM bright field and dark field images to observe defect type and its distribution and SAD (selected-area-diffraction) to determine the lattice structure.

2.3.2 ESCA

X-ray Photoelectron Spectroscopy known as XPS or ESCA (Electron Spectroscopy for Chemical Analysis) has been developed from the Fifties by Professor K. Siegbahn. The Physics Nobel Prize was awarded to his work in 1981.

The most interesting thing with this technique is its ability to measure binding energy variations resulting from their chemical environment. That is, information on the chemical nature and state of the detected elements at the sample surface. The theory of determination of

chemical bonding of ESCA is based on the equation below:

$$BE(i)=l(i) + qk(i) +\sum V(ij) + Er(i)$$

i: the electron orbit which emits the photoelectron***, BE(i):***total binding energy ***,l(i) :***binding energy at neutral condition(element) ***,q: charge, K(i)***:constant***,*** ***Er(i):***relaxation energy***, V(ij):*** electron potential energy from other atoms within the molecule

When atoms are bonded, valence electrons will form the bonds and the energy states of atoms will change and the atoms may deviate from neutral. The difference in electron affinities will make some atoms more positive charged than neutral and others more negative charged. The positive charged q added the total binding energy and peak shifts to higher binding energy, and vice versa. The higher oxidation state has higher electron binding energy since it is more positive. As a result, ESCA is a powerful tool to study the chemical bonding and oxidation state.

The basis of ESCA is X-ray induced photoemission. When the specimen atom absorbs a photon from the X-ray source, it gains the energy of the photon and release a photoelectron to regain its original stable energy state. The released electron retains all the energy from the striking photon. It can then escape from the atom, and even further from matter and kinetic energy keeps it moving. Which can be described by the following equations :

$$E_{ph}= h\nu - E_z$$

E_{ph} is the kinetic energy of photoelectron, hv is incident X-ray photon energy, E_z is the binding energy of specimen atom. As for solid state material, work function Φ is added to represent the energy of an electron

escape from the surface. Hence the equation is modified as below:

$$E_{ph} = h\nu - E_z - \Phi$$

The incident photon energy of usual X-ray sources used in ESCA are Al Kα 1486.6 eV and Mg Kα 1253.6 eV. In our experiment we use the Al Kα X-ray source with a Rowland circle, which is a set of bended quartz crystal to reflect the source X-ray to the specimen thus we can avoid the Al $K\alpha_3$ satellite line appear on the spectrum and the FWHM of peak is also reduced .

Besides the X-ray induced photoelectron signals, consequently, there will be some atoms lacking electrons in the internal shells from which photoelectrons have been released. To recover from this ionized state the atom can emit another photon (fluorescence) or undergo an Auger transition and result in Auger electron signals. We must tell from the two kinds of signals in the spectrum. One way to distinguish these two kinds of peaks is to change the X-ray source since the Auger electron kinetic energy is independent of the source but the photoelectron kinetic energy is depending on the source. In our experiment we focus on specific element peak instead of total scan, therefore, we use the reference book directly distinguish the Ga Auger peak near the O_{1s} XPS peak and eliminate it.

There is a severe problem called "charging" occur among insulator and wide bandgap semiconductors. While the photoelectrons escape from specimen, if there aren't enough electrons flow into specimen to maintain electrical neutrality. The specimen tends to be positively charged and result in a peak shift toward higher binding energy. We can use a flood gun to inject low energy electrons to the surface to

neutralize the charge. But many times it is not that simple to solve the problem. Charging may be inhomogeneous and has spatial distribution for insulator. How to modify the flood gun current sometimes is not very easy. The worst situation happens when Ar ion sputtering used for depth profiling of insulators. Ar ion is charged and may react with the surface thus we can't identify the cause of peak-shift. Coating a thin conducting film on insulating specimen and ground it could be an effective way to avoid charging. We can also take $Au_{4f7/2}$ peak at 83.86eV as a reference while scanning.

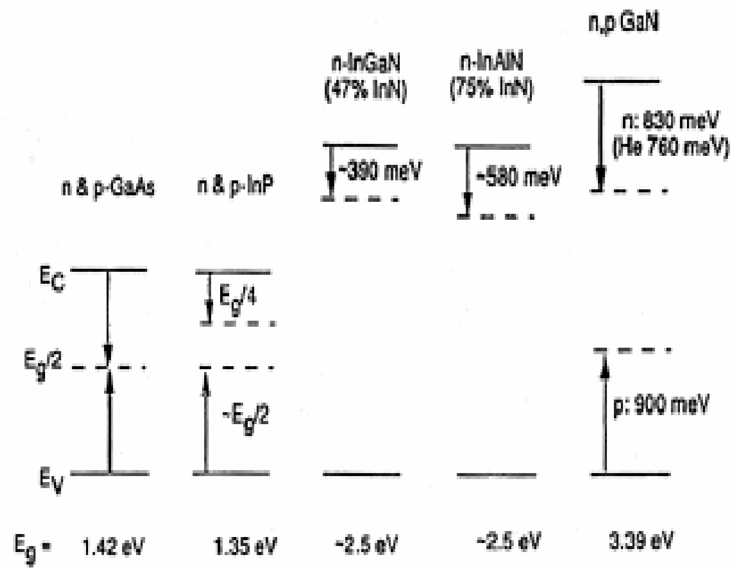

Figure 47. Schematic representation of the position in the energy gap of compensating defect levels from implant isolation in GaAs, InP, $In_{0.47}Ga_{0.53}N$, $In_{0.75}Al_{0.25}N$ and GaN.

Fig.1 Defect levels estimated from Arrhenius plots

Chapter 3

Test Process, Device Fabrication and Material Analysis

Sample Preparation and Measurement

3.1 Test Process

Before real device processing, we first estimated the implantation isolation effects to make sure whether it will work or not. We deposited Ti/Al/Ni/Au metal pads on wafer by evaporator and then RTA it to form ohmic contacts. We got six pads in a row and the spacings between pads are 3, 5, 10, 20 and 36 microns. The width of the row is 75 um. After ohmic contact formation, ICP was applied to etch the epi-layer to 2500um depth outside the row to make sure the current between ohmic contacts were confined within the row. We measured the currents between ohmic contacts of each spacing and recorded it. Before multi-energy oxygen ion implantation, TRIM software simulation was applied to determine the implantation energy. After that, we send the wafer to National Central University for multi-energy oxygen ion (O^{2+}) implantation. Then we measured the currents after implantation to estimate the implantation isolation effect. Considering real device fabrication, passivation is carried at 250~300℃ for about 30 minutes. We had also considered implant before ohmic contact formation in order to achieve insulating areas under metal pads and see if it will result in better RF performance. If we do so, implantation isolation must resist RTA temperature up to 800~900℃. Therefore, besides measurement just after implantation, we also tube annealed the samples at different temperatures for 1 hour and then measured the currents between pads to see whether the isolation quality

degrades or not after passivation or RTA.

There is another important thing we must take into consideration: What can we use for the mask of implantation during device processing? The active region must remain undamaged during implantation process and the mask must be easily removable after implantation. So we took thick photoresists into consideration. AZ5214E photoresist was first tried, but unfortunately, it will be burned after implantation and become hard to remove. Than we used another photoresist as implantation mask to cover the row of metal pads and hard bake to enhance cross-linking. Then we ion implanted it at the same condition as above. After implantation, the photoresist mask was removed by immersing the sample into ACE and shaking it with ultrasonic vibration. Then we measured the saturation currents between ohmic contact pads to see if the photoresist covering could protect the active region from ion bombardment.

3.2 Device Structure

The schematic cross-sectional view of our AlGaN/GaN HEMT structure was shown in Fig.1. The wafer was grown by MOCVD epitaxy on sapphire substrate along (0001) axis. It is wurtize structure. The layer sequence consists of a 3um undoped GaN layer at bottom and 30nm undoped AlGaN layer with Al composition of 0.3 at top. And the 2-dimensional electron gas was located about 10nm below AlGaN/GaN interface in the GaN region. The sheet carrier concentration was $1*10^{13}/cm^2$ and electron mobility was $1300cm^2/V.S.$ at 2DEG.

3.3 Device Fabrication

1. Wafer cleaning

First, in order to remove the undesired particles and contaminations from surface layer, the wafer was immersed in ACE and then IPA for each five minutes. And then D.I water rinsed and N_2 blew dry. After that, the wafer was immersed into HCl and H_2O mixed solution for five minutes to remove the surface oxide for better ohmic contact. Then D.I rinsed and N_2 blew dry again.

2. Ohmic contact formation

First, we used lithography process to define the ohmic contact region. Then the wafer was immersed into HCl and H_2O mixed solution for five minutes to remove the surface oxides. Ti/Al/Ni/Au was deposited layer by layer with evaporator onto the lithography patterned wafer. And ACE lift-off process was applied to remove the unwanted metal then leave source and drain contact electrodes. RTA process was carried out at 800℃~900℃ for about 1 min.

Finally, we used HP4142 and HP4156 to measure the ohmic contact resistance and current between source and drain before T-gate formation.

3. Implantation Isolation

After ohmic contact formation, we used photoresist to cover the active region from ion bombardment. The photoresist was hard baked to enhance cross-linking. The wafer was send to NCU for 180+90+75+30keV sequence multi-energy oxygen ion implantation. The total ion dose is $2*10^{15}/cm^2$, $5*10^{14}/cm^2$ for each implantation energy. The photoresist mask was removed by immersing into ACE and ultrasonic shaking for 5 minutes. Then it was dipped into IPA

and N_2 blew dry.

4. T-Gate Formation

To obtain a T-gate, we used a double photoresist structure consisting of PMMA for the bottom layer and PMMA-MMA for the top layer. After cleaning, PMMA and PMMA-MMA were coated and baked layer by layer. E-beam direct writing was applied to form a T-shape region by different exposing width of the top PMMA-MMA layer and bottom PMMA layer after Al coating. The Al thin film was removed by FHD-5 immersing for 1 minute. Then the photoresists were developed and left a T-shape region. Then gate metal Ni/Au was consequently deposited layer by layer by evaporator. After evaporation, the wafer was immersed into ACE to lift-off the metal and then dip into IPA and N_2 blew dry.

5. Device Passivation

After T-gate formation and DC measurement, the wafer was passivated with 1000 Å Si_3N_4 grown by PECVD. Then RIE was applied to open nitride via at the contact pad region. After passivation and nitride via, HP4142 and HP4156 was applied for DC measurement.

3.3 Material Analysis Sample Preparation and Measurement

3.3.1 TEM Sample Preparation and Measurement

First, we cut the sample into 2mm*5mm small pieces. Then we cleaned it with ACE and IPA. We used G1 epoxy to bind two pieces epi-layers face to face together. Therefore, we could obtain a cross-section of two epi-layers together. Then we polish it for thinning

and put it on the Cu-ring. Again ACE and IPA were applied before ion-milling to remove organic contaminations, which will result in dark carbon spot on sample while ion-milling. We use PIPS ion-miller and Ar ion source for ion-milling. Ar ion-milling mainly depends on physical ion polishing. As a result, it will cause some damage on the sample. Fortunately, the ion energy for implantation and ion milling is largely different. We could eliminate the possibility for taking ion milling caused damages as ion implantation caused damages.

After sample preparation, we used Philips TECNAI 20 at material science and engineering department of NCTU and JEOL JEM 2010 FX at NDL to take TEM images.

3.3.2 ESCA Sample Preparation and measurement

First, we immerse the sample into ACE for 5minutes. Then the sample was dip into IPA for 1 minute and N_2 blow dry. After that, a $HCl:H_2O$ =1:10 solution was applied to remove the surface oxide. And then D.I water rinse and N_2 blow dry. During ESCA measuring, peak position may shift because of local surface charging for non-conducting samples. To distinguish from real chemical-shift and charging-shift, there are two important things need to be done while sample preparing. After we had cleaned the sample, first, we use evaporator or sputter to deposit a very thin Au film for conducting; second, we use Hall mask to deposit an Au spot on sample for referencing.

After sample preparation, it was send to chemical department of National Taiwan University using VG Scientific ESCALAB 250 for ESCA measurement. We first scan the Au spot $Au4f_{7/2}$ peak at 83.86eV for referencing and calibrate the flood gun. Then we scan $Ga2p_{3/2}$, O1s

and N 1s peaks at the surface. After surface scanning, Ar sputtering was applied for depth profiling. We scan every 150Å layers to 1200˚ A to see the distribution and changes in different depths. The XPS core-level peaks were deconvolved into their various components by using an interactive least-squares computer program, the curves being taken 80% Gaussian and 20% Lorentzian mixed function.

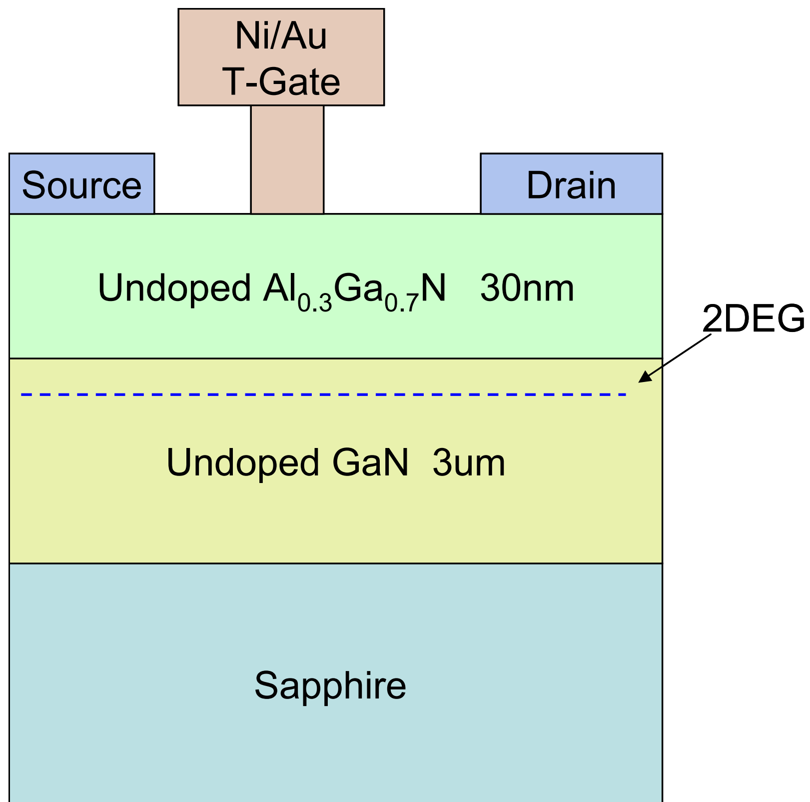

Fig. 1 AlGaN/GaN HEMTs Device structure

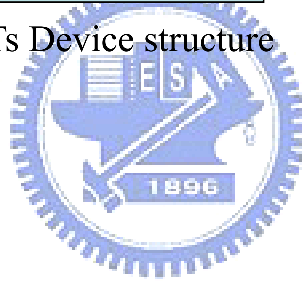

Chapter 4

Result and Discussion

4.1 Electrical Results and Discussions

4.1.1 Isolation Results

Isolation quality versus 1hr post-annealing temperature was in Fig.1. We could see that 200~300°C 1hr post-annealing made isolation quality better than the as-implanted sample. The lowest leakage current between two 75um width ohmic contacts at 5um spacing was 250pA at 20V bias for 300℃ 1hr post-annealed sample. It is extremely small when compared with ICP mesa etched samples, which reveals a 30uA leakage current at the same contact width and spacing.

Isolation quality degraded as temperature increased up to 850°C, but it turned a little bit better at 950°C.

4.1.2 DC Characteristics

We measured DC characteristics of 80um gatewidth multi-energy oxygen ion implant isolation AlGaN/GaN HEMTs with gate length 0.4um, 1.5 gate-source spacing and 1.5um, 2.5um, 3.5um and 4.5um gate-drain spacing before and after passivation. After passivation, the source-drain saturation currents of 1.5um, 2.5um, 3.5um and 4.5um gate-drain spacing AlGaN/GaN HEMTs were 673.5mA/mm, 607mA/mm, 538mA/mm and 528mA/mm. The peak extrinsic transconductance, gm, are 288mS/mm, 245mS/mm, 145mS/mm and 180mS/mm. Typical DC transconductance of a 80um gatewidth multi-energy oxygen ion implant isolation AlGaN/GaN HEMTs with gate length 0.4um and 1.5um gate-drain spacing after passivation was shown in Fig.2. The maximum

transconductance, Gm_{max}, of approximately 288mS/mm was measured at gate bias of -1.6V and at a drain bias of 6V. The channel pinch off voltage was -5.0V. Typical I-V characteristics were also shown in Fig.3. The source-drain saturation current, Idss, at Vgs=0V, was 673.5mA/mm. The ohmic contact resistance was $5.96*10^{-6}\ \Omega/cm^2$. The channel pinch-off is about -5V. The knee voltage measured at 1V gate bias was 4.8 V.

We also showed typical I-V characteristics of a 4.5um gate–drain spacing multi-energy oxygen ion implant isolation AlGaN/GaN HEMTs after passivation in Fig.4. Compare with 1.5um gate-drain spacing, it is clear that current slump is suppressed for 4.5um gate-drain spacing. It is because the gate-drain electric field is weaker for 4.5um gate-drain spacing device. As a result, hot channel effect is reduced for lower electric field. Lower electric field also resulted in fewer electron attracted from 2DEG to the near gate region between gate and drain. Virtual gate mechanism, which means the accumulation of electrons at the near gate surface region that depletes the channel like a gate, is also suppressed. Therefore, current slump is reduced.

Typical I-V characteristics of a 4.5um gate-drain spacing ICP mesa etched isolation AlGaN/GaN HEMTs after passivation shown in Fig.5 were also taken for comparison of a 4.5um gate-drain spacing multi-energy oxygen ion implant isolation AlGaN/GaN HEMTs. From this figure, current slump is suppressed for ion implantation isolation HEMTs. Saturation current also improved from 438mA/mm to 528mA/mm. We suggested that the improvement of saturation current may result from less virtual gate effect. Ion implantation isolation HEMTs do not have gate metal lines at the mesa edge to draw electrons

from 2DEG to the near gate surface region. It resulted in less charge accumulation at the near gate surface region.

The I-V characteristics of before passivation 4.5um gate-drain spacing multi-energy oxygen ion implantation and ICP mesa etch isolation AlGaN/GaN HEMTs were shown in Fig. 6 and Fig.7. For ICP mesa etch isolation AlGaN/GaN HEMTs, the before passivation devices exhibited severe current slump behavior. After passivation, current slump behavior of ICP mesa etch isolation AlGaN/GaN HEMTs was highly suppressed. On the contrarily, suppression of current slump behavior was not significant for multi-energy oxygen ion implantation isolation AlGaN/GaN HEMTs. Ion implantation isolation resulted in less electron flew from 2DEG to near gate surface region and reduced virtual gate effect.

Breakdown and reverse-bias gate leakage current measurement were carried on both 4.5um gate-drain spacing multi-energy oxygen ion implantation isolation and ICP mesa etch isolation AlGaN/GaN HEMTs. The AlGaN/GaN HEMTs using implantation isolation exhibited a higher off-state breakdown at 80V (1mA/mm drain current) than those using ICP mesa etch isolation exhibited a off-state breakdown at 42V. Gate-drain breakdown was 87V (1mA/mm drain current) for implant isolation AlGaN/GaN HEMTs and 50V for ICP mesa etch AlGaN/GaN HEMTs. Since off-state breakdown value is close to gate-drain breakdown, we suggest that surface breakdown dominates rather than channel breakdown. Leakage current between gate and drain pad was suppressed for implantation isolation. Therefore, a higher gate-drain breakdown was obtained. Reverse-bias gate leakage current was 1mA/mm at Vg=-53V

for implant isolation AlGaN/GaN HEMTs and at Vg=-27.5V for ICP mesa etch AlGaN/GaN HEMTs. The above values were listed in Table .1 for comparison.

4.2 Material Analysis Results and Discussion

4.2.1 TEM Results and Discussion

We had tested multi-energy oxygen ion implantation isolation quality before and discovered that wafer quality is critical for isolation. Due to the 13% lattice mismatch of GaN and sapphire, threading dislocation generates at the GaN/sapphire interface and penetrate toward the surface. If the threading dislocation density is too high, leakage current may flows through dislocation. From Fig.8.9.10, the density of threading dislocation was not high in our sample and usually annihilated in the bulk region instead of penetrated to the surface. As a result, we could eliminate the bulk leakage current at our isolation test. Based on our isolation test results shown in Fig.1, after implantation, 300℃ 1hr post-annealing made isolation result even better than the as-implanted sample. The isolation effect degraded as post-annealing temperature increases up to 850℃. As a result, we took XTEM pictures for un-implanted, as-implanted, 300℃ 1hr post-annealed, 850℃ 1hr post-annealed samples since these conditions reflected the changes in isolation effects.

1. ***Un-implanted***

   First, the bright field image of the before implant sample at 97,000 magnification (Fig. 11) taken by Philips TECNAI 20 at the MSE

department of NCTU showed only two crystal-growth related line defects from the surface. No point defect or cluster was observed.

2. ***As-Implanted***

After multi-energy oxygen ion implantation, the 100,000 magnification bright field image (Fig.12) taken by JEOL JEM 2010FX at NDL clearly showed the distribution of ion implant induced point defects. Due to ion milling, the as-implanted sample was a little bit bended and resulted in the unwanted black shadows on the picture. It was likely the cause of thickness fringes. We could tell these kinds of shadows and thickness images from real images by moving the sample. Since the shadows will move but real images won't. From this image we also saw that the point defects were a little bit clustered due to heating while ion-milling. The distribution of implantation induced defects was from surface to about 3000Å, which matched our TRIM software simulation and was effective for isolation because the 2DEG of AlGaN/GaN HEMTs was only 400 Å in depth.

3. ***Implanted and Post-Annealed 300℃ 1hr***

After multi-energy oxygen ion implantation and 300℃ 1hr post-annealing, the 175,000 and 250,000magnification bright field image (Fig. 13. 14) taken by Philips TECNAI 20 at MSE department of NCTU clearly showed the point defects further clustered and grown into planar defects parallel to the basal plane. Since defects were further clustered, the distances between defects were increased. As a result, hopping conduction between defects was reduced and isolation effect got better at this condition.

Implantation induced planar defects had been reported in [10] for 40 keV C ions with $8*10^{15}/cm^2$ ion dose at LN2 implantation temperature. But microstructure and formation mechanism of these planar defects were not understood. There was a very smooth interface between the crystalline GaN with planar defects at bottom and the bright transparent amorphous GaN at top. The planar defects at the interface seemed growth along the basal plane and connected each other to be continues at the interface plane. As seen in Fig. 15. And it turned to be the nucleation site for amorphous GaN if further energy was applied. As a result, layer-by-layer growth of amorphous GaN occurred at the interface. As the mechanism which was reported in for $2*10E14/cm^2$ 100keV Au ions bombardment at RT [10]. This mechanism may explain why the interface between crystalline and polycrystalline GaN was atomic smooth for the lattice image we took from 850℃ 1hr post-annealed sample (Fig. 16). Atomic smooth interface had also been discovered at plasma immersion ion implantation SOI (silicon on substrate) [11]. The oxygen implantation induced SiO_2 layer also has an atomic smooth interface with the upper silicon. And the SOI implantation temperature is about 550~600℃. The mechanisms of these two atomic smooth interfaces maybe have something in common.

4. ***Implanted and Post-annealed 850℃ 1hr***

After multi-energy oxygen ion implantation and 850C 1hr post-annealing, the 100,000 magnification bright field image

(Fig.17) taken by JEOL JEM 2010FX at NDL showed a single crystalline GaN with defect clusters at the bottom and a polycrystalline region at the top. Dark Field image of Fig.17 was also applied (Fig.18). With polycrystallization from amorphous matrix, leakage currents flowed through grain boundary and further degraded isolation effects. The interface between single crystalline GaN and poly crystalline region was atomic smooth at 600,000 magnification lattice image (Fig.16). To determine the phase and structure of the polycrystalline region, we use SAD (selected-area-diffraction) to fond out the lattice constant values (d_{hkl}) of the rings (Fig. 19). The lattice constants (d_{hkl}) were 1.31A, 1.55A, 2.18A and 2.52 A. After checking JCPDS , hexagonal GaN revealed four strong diffraction peaks at 1.31A, 1.55A, 2.18A and 2.52A lattice constants (d_{hkl}). The polycrystalline region was proofed to be polycrystalline GaN. Results from Refs. [12] showed that thermal annealing of amorphous GaN at temperatures above ~ 500oC resulted in polycrystallization rather than in solid phase epitaxial growth (SPEG). Thus, we can say the polycrystalline GaN region may come from polycrytallization of the already existed amorphous GaN during thermal annealing. Lattice image at 600,000X also showed the precipitation of grains from amorphous matrix (Fig.20). And STEM images of as-implanted and 850C 1hr post-annealed samples clearly showed the thickness of polycrystalline region of 850C 1hr post-annealed sample was the same as implantation induced defects region of as-implanted sample (Fig.21). Amorphourization and polycrystallization only occur at

implantation damaged region since it was energetically favorable.

4.2.2 ESCA Results and Discussion

We had measured four samples: GaN single crystal before implantation, as-implanted, 850℃ 1hr post-annealed and 950℃ 1hr post-annealed samples to discover the bonding conditions of Ga-N and implanted O^{2+}. The reference peak value of $Ga2p_{3/2}$ for GaN was hard to obtain. It was not available in the ESCA handbook. From Ref [13], [14] and [15], Ga2p3/2 peak located from 1115eV to 1117.1eV. And O1s peak for O-Ga bonding located at 530.8eV. We illustrated the results of $Ga2p_{3/2}$ for un-implanted, as-implanted and 850℃ 1hr post-annealed samples in Fig. 22. From this graph, it was clear that the $Ga2p_{3/2}$ binding energy peak shifted from 1118.38eV to 1120.5eV after implantation. This is because ion implantation damaged lattices and induces lattice distortion of the GaN matrix as seen in the HRTEM lattice image of as-implanted GaN (Fig. 23). Implanted oxygen ions mainly occupied interstitial sites before thermal annealing and caused lattice distortion. Implantation induced compressive stress field also had been reported in [16] As a result, inter-atomic spacing may change and affected Ga-N bonding condition which resulted in the shift of Ga2p3/2 peak towarded higher bonding energy. The binding energy of Ga2p3/2 shifted back to 1118.5eV after 850℃ 1hr annealing because thermal annealing could release the lattice distortion and stress. Oxygen atoms at interstitial sites also thermally activated to occupy substitial sites after thermal annealing. Some extent of lattice distortion and stress were also released. There is no significant change for 850℃ and 950℃ post-annealed sample as seen

in Fig.24. The Ga2p3/2 peaks of all samples were very narrow in FWHM (1.09eV) and could be regard as single bonding peak. Ga-O bonding didn't been discovered, or, below the detection limit and couldn't be separated from Ga-N peak.

We also illustrated the results of O1s peaks of un-implanted, as-implanted and 850℃ 1hr post-annealed samples in Fig.25. For un-implanted sample, O 1s peak located at 532.9eV. It is consisted of the O-H peak at 533.1eV and O-Ga peak at 530.8eV. After O^{2+} ion implantation, the O1s peak shifted a little bit to higher energy at 533.5eV because there was a small peak of implanted unbonded O^{2+} at higher binding energy. After 850℃ 1hr post-annealing, the small peak of implanted unbonded O^{2+} is eliminated and O1s main peak shifted back to the original position of un-implanted sample. This could be explained that 850℃ 1hr post-annealing thermally activated implanted O^{2+} from interstitial position to substitute N and bonding with other atoms. Thus the peak of implanted O^{2+} ion was eliminated. We can not tell any significant difference for O1s peaks of 850℃ and 950℃ post-annealed samples as seen in Fig.26.

The results of N1s peaks for un-implanted, as implanted and 850℃ 1hr post-annealed samples were illustrated in Fig.27. The N1s bonding energy peak located at 397.5eV. No significant change is absorbed.

4.2.3 AFM Results and Discussion

AFM measurements of root-mean square surface roughness for un-implanted, as-implanted and 950℃ 1hr post-annealed samples were

shown in Fig. 28, Fig. 29 and Fig. 30. No significant change in surface roughness was discovered. The root-mean-square surface roughness remained less than 1nm for all samples. Planarization was not degraded after implantation and post-annealing.

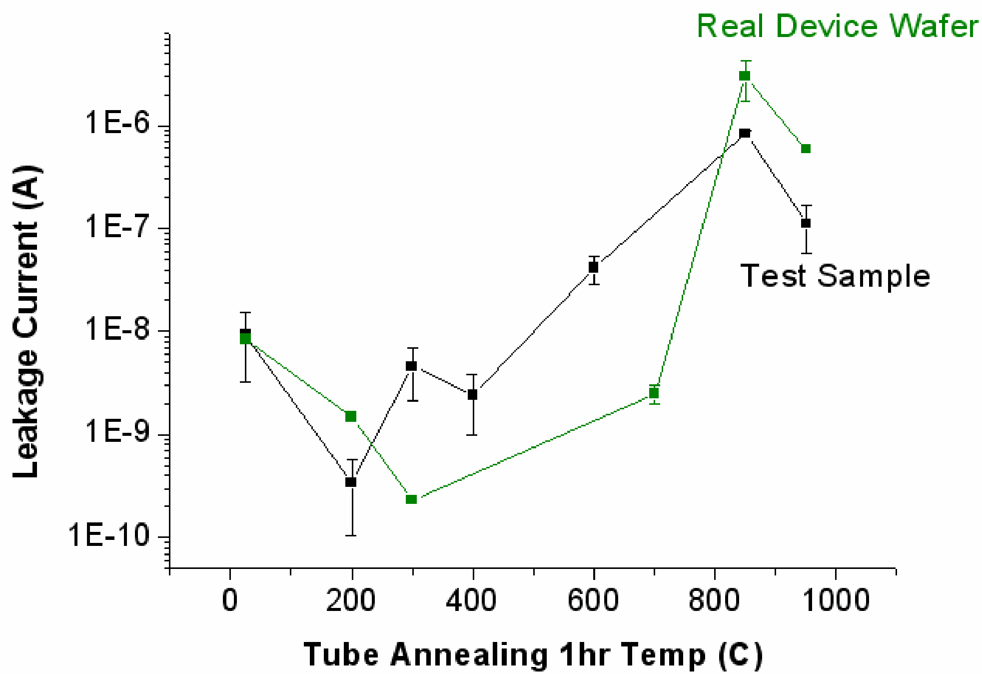

Fig.1 Isolation quality test results. The leakage currents were measured between ohmic contact pads of 75um width and 5um spacing

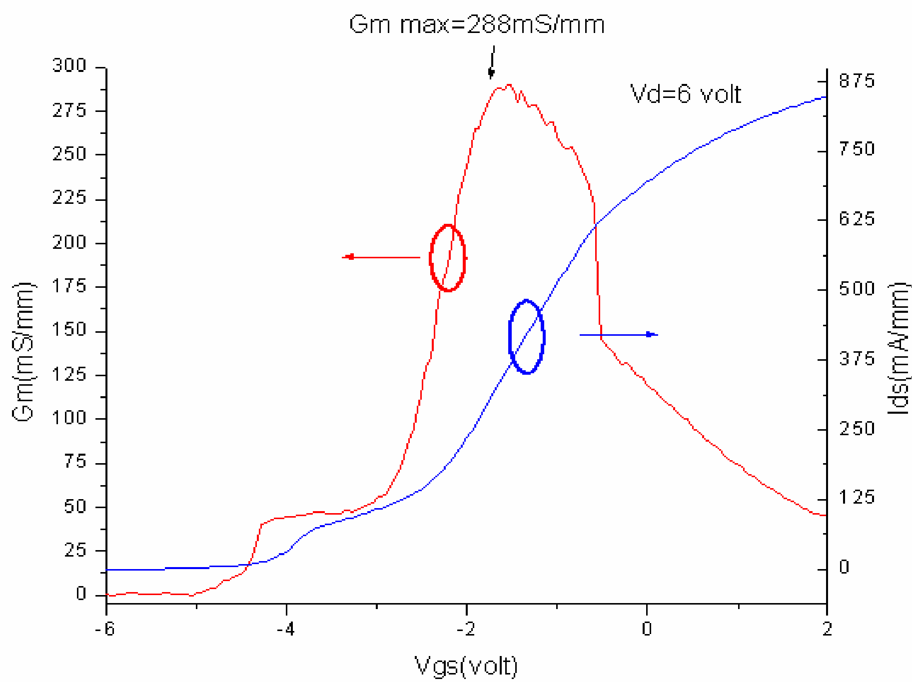

Fig.2 Typical DC transconductance of a 80um gatewidth multi-energy oxygen ion ***implantation isolation*** AlGaN/GaN HEMTs with gate length 0.4um and ***1.5um gate-drain spacing after passivation***

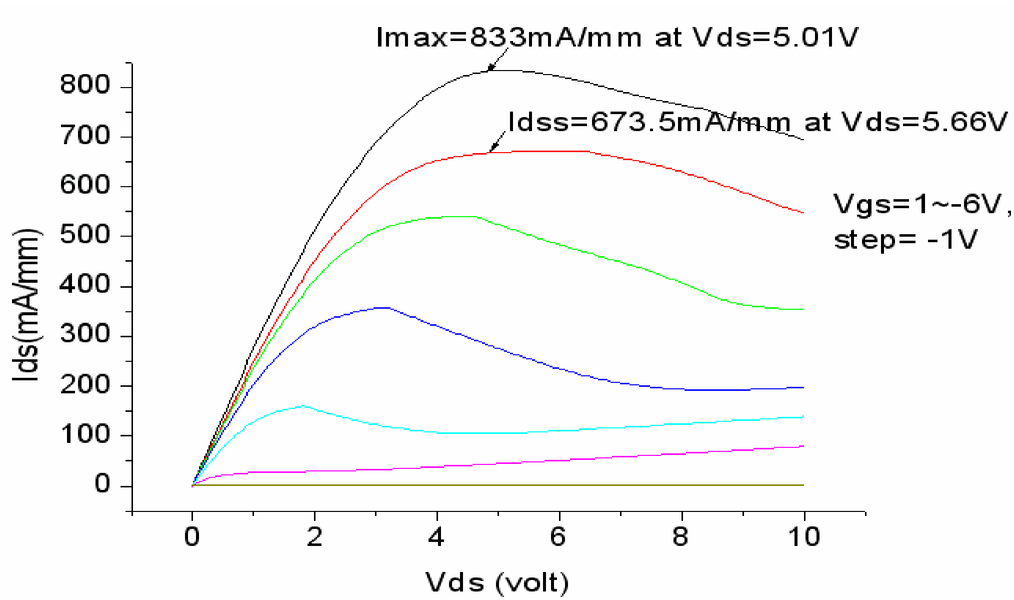

Fig.3 Typical I-V characteristics of a 80um gatewidth multi-energy oxygen ion ***implantation isolation*** AlGaN/GaN HEMTs with gate length 0.4um and ***1.5um gate-drain spacing after passivation***

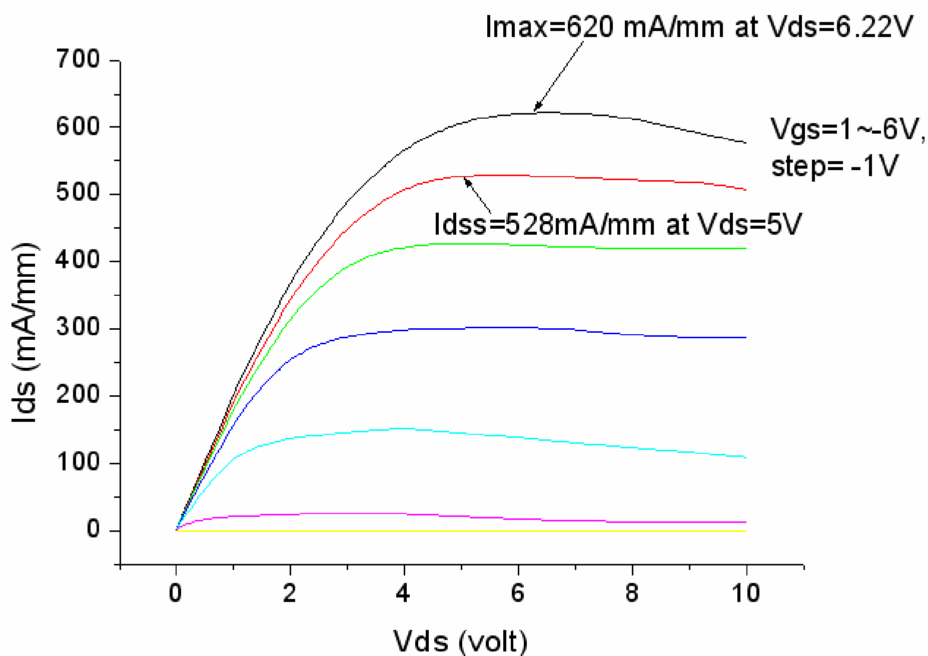

Fig.4 Typical I-V characteristics of ***4.5um gate–drain spacing*** multi-energy oxygen ion ***implantation isolation*** AlGaN/GaN HEMTs ***after passivation***

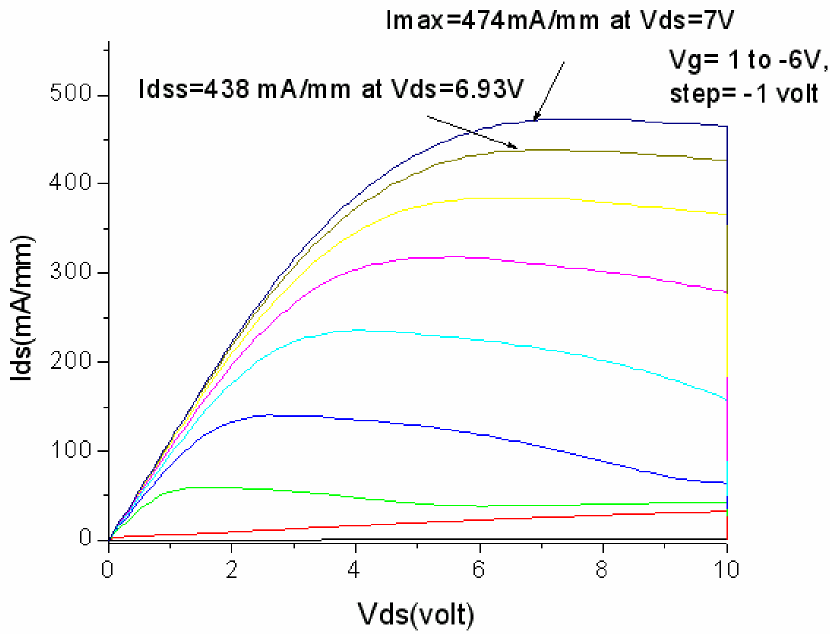

Fig.5 Typical I-V characteristics of a ***4.5um** gate-drain spacing ICP*
mesa etched isolation AlGaN/GaN HEMTs ***after passivation***

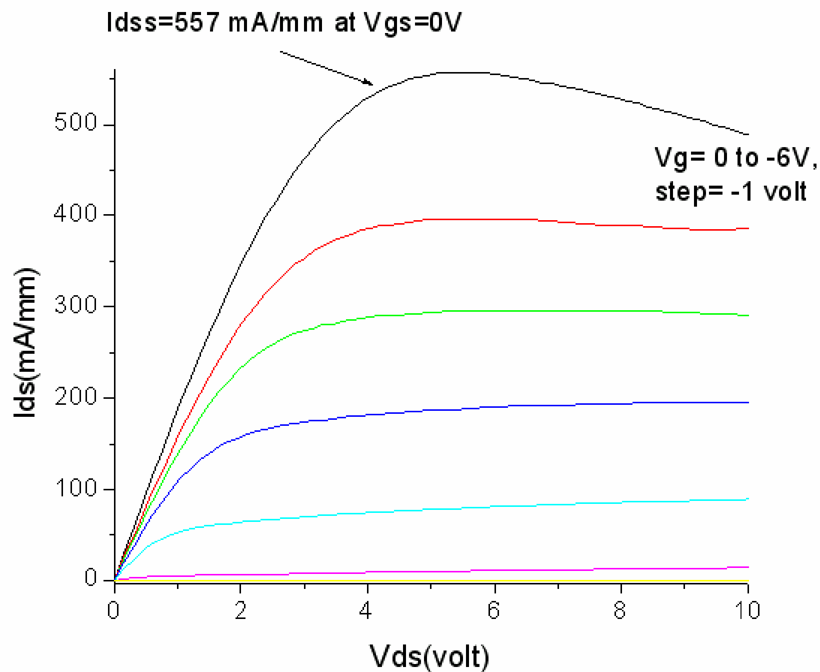

Fig.6 I-V characteristics for the ***before passivation*** 4.5um gate-drain spacing multi-energy oxygen ***ion implantation*** isolation AlGaN/GaN

HEMTs

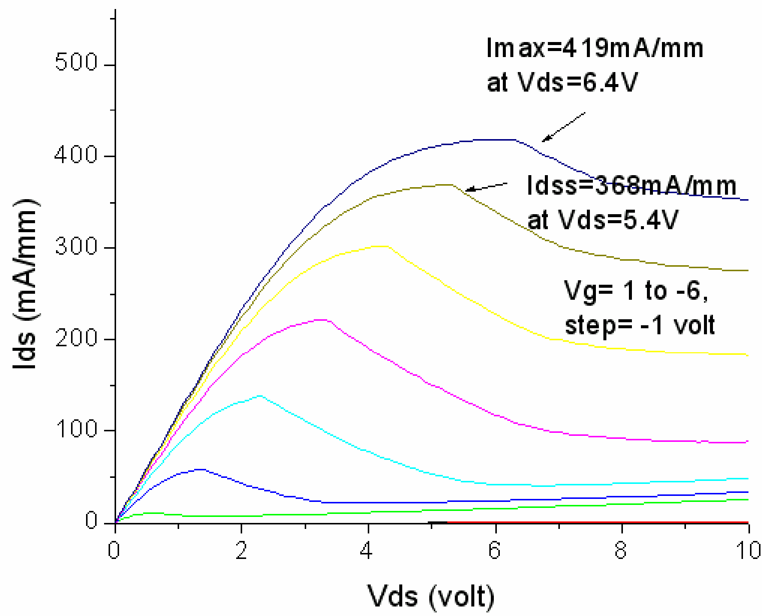

Fig.7 I-V characteristics for the ***before passivation*** 4.5um gate-drain spacing ICP ***mesa etch*** isolation AlGaN/GaN HEMTs

Table.1 breakdown comparison

	Implant isolation AlGaN/GaN HEMTs	ICP mesa etch isolation AlGaN/GaN HEMTs
off-state breakdown (Id=1mA/mm)	80V	42V
gate-drain breakdown (Id=1mA/mm)	87V	50V
Vg for reverse-bias gate leakage current at 1mA/mm	-53V	-27.5V

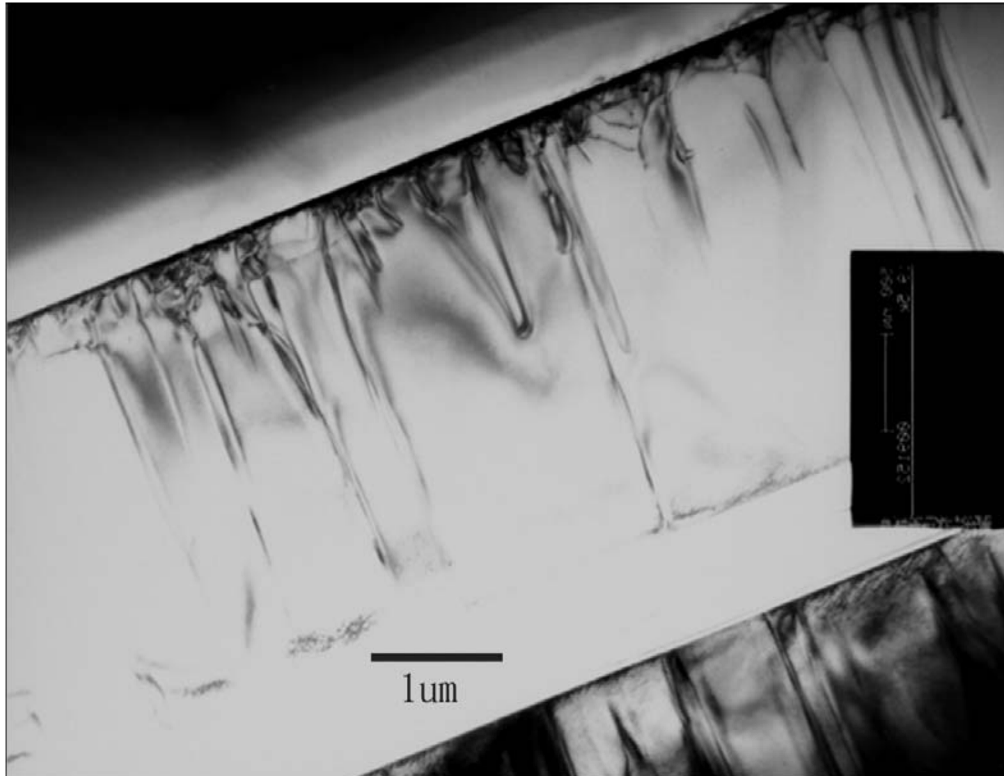

Fig.8 BF image of the epi-layer structure used in this study

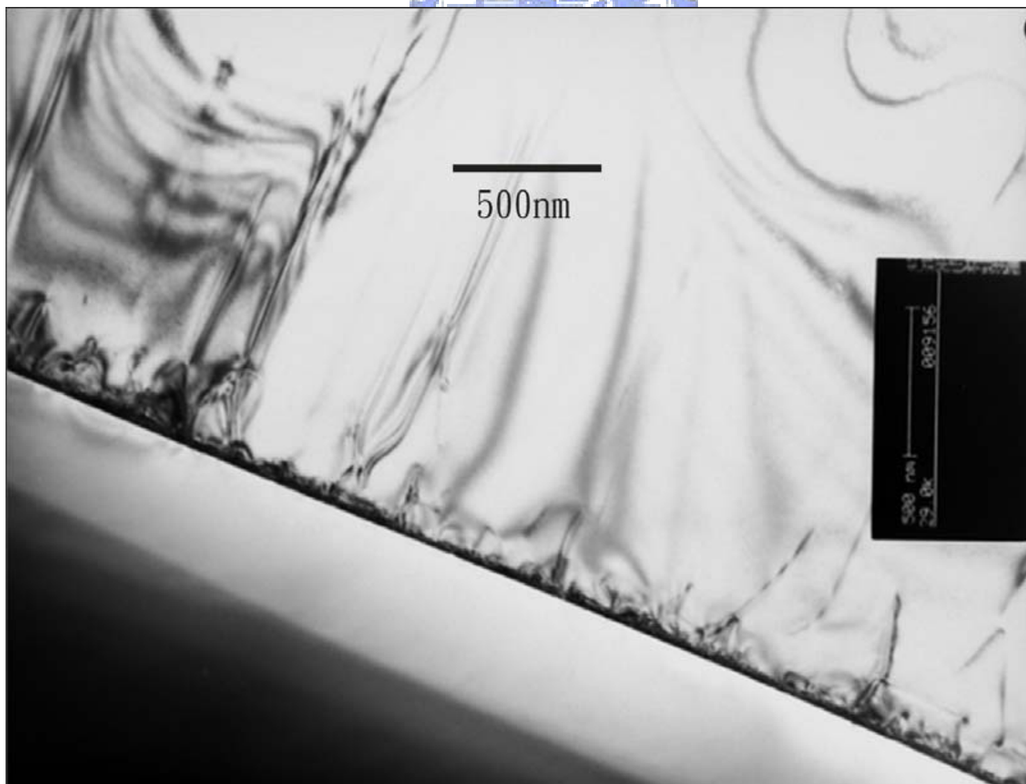

Fig.9 BF image of sapphire/GaN interface

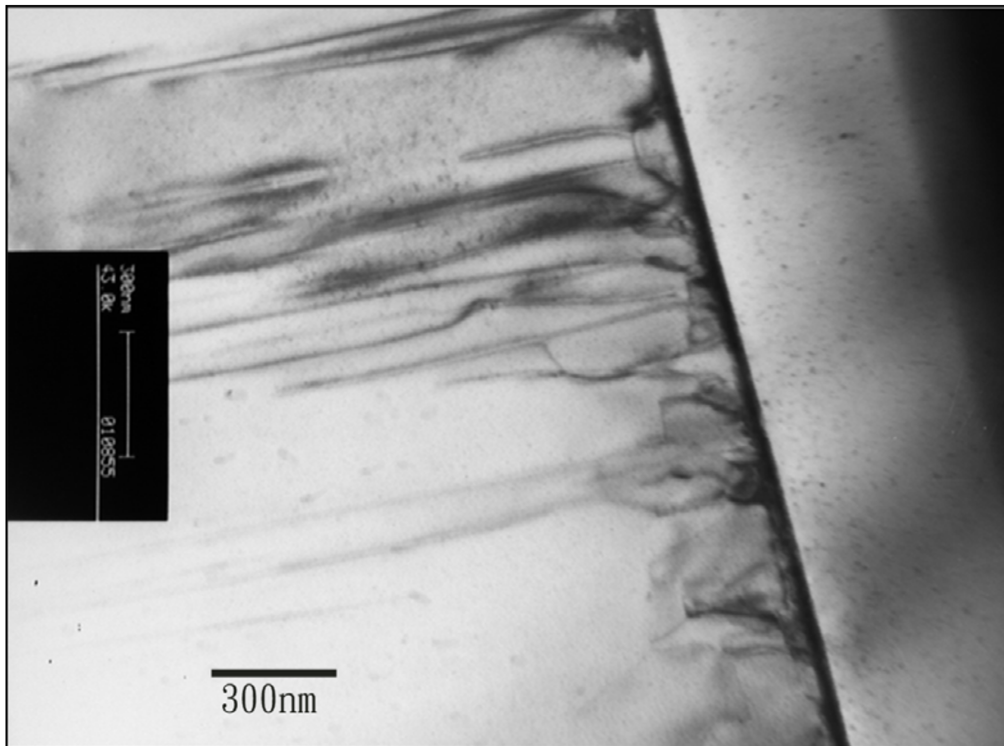

Fig.10 BF image of the sapphire/GaN interface

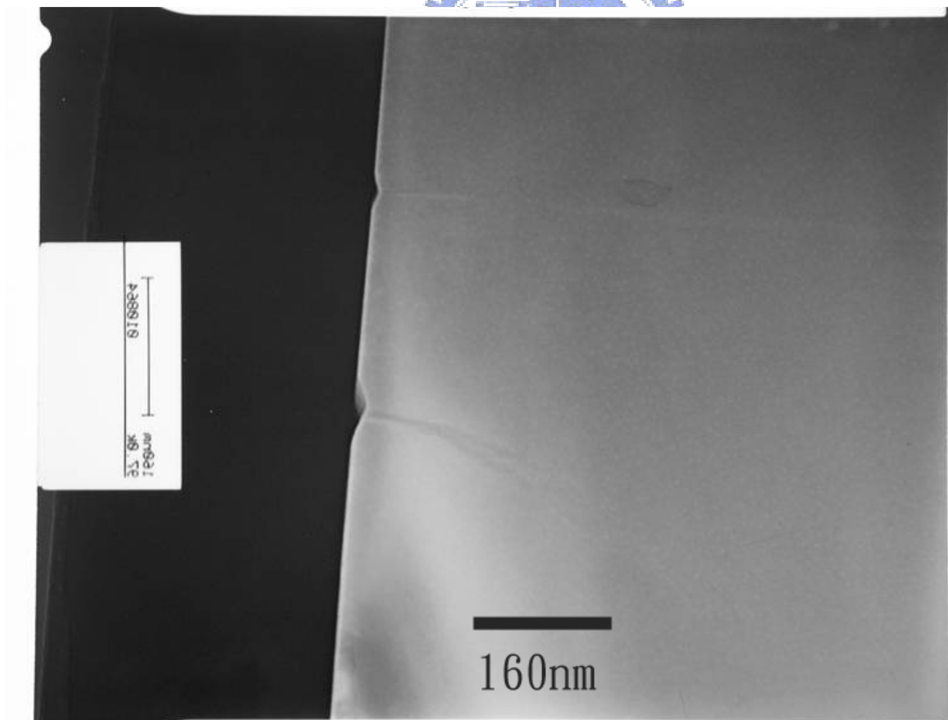

Fig.11 97K BF image of the un-implanted sample

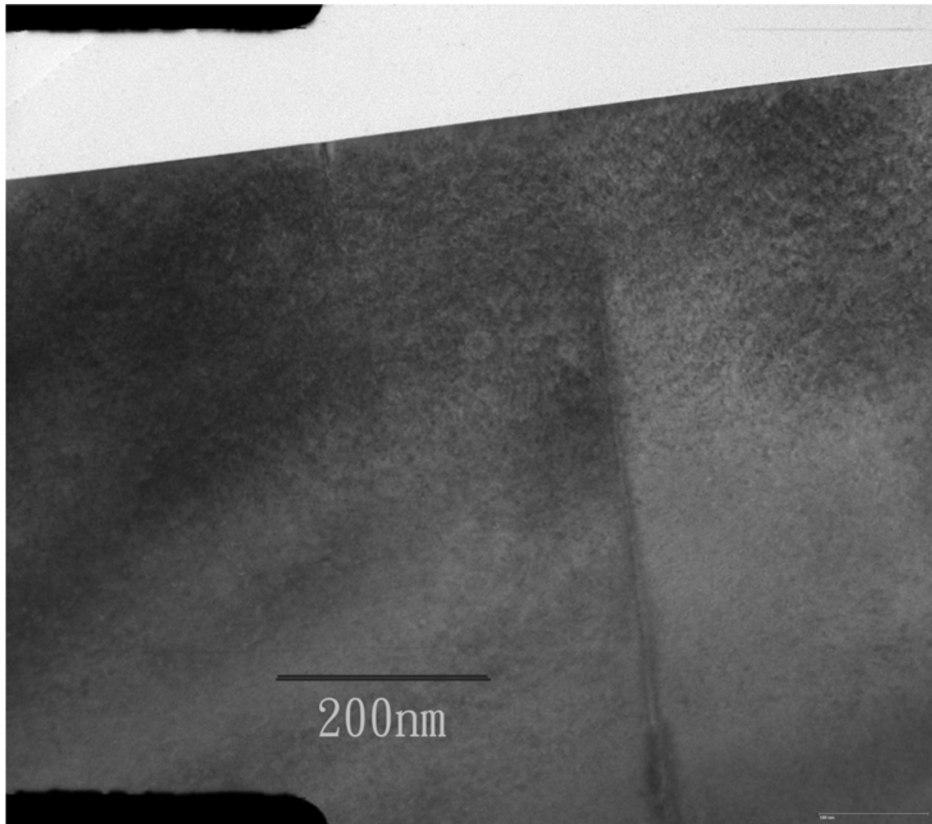

Fig.12 100K BF image of the as-implanted sample

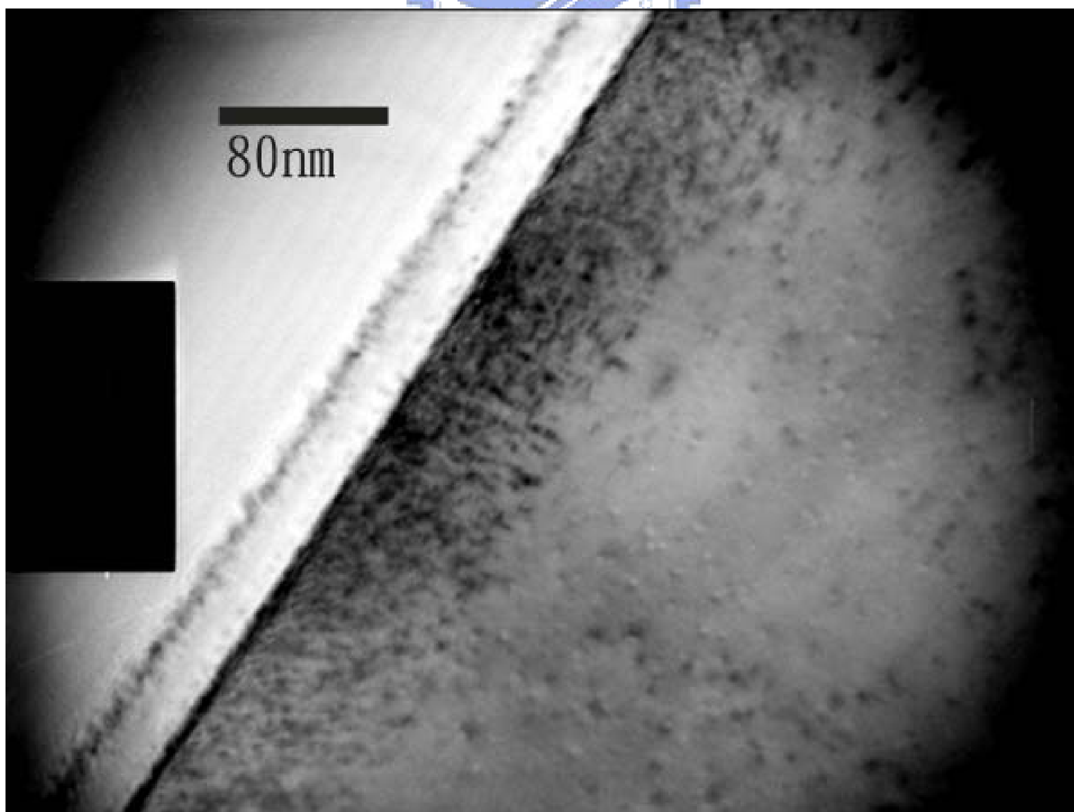

Fig.13 175K BF image of the 300℃ 1hr post-annealed sample

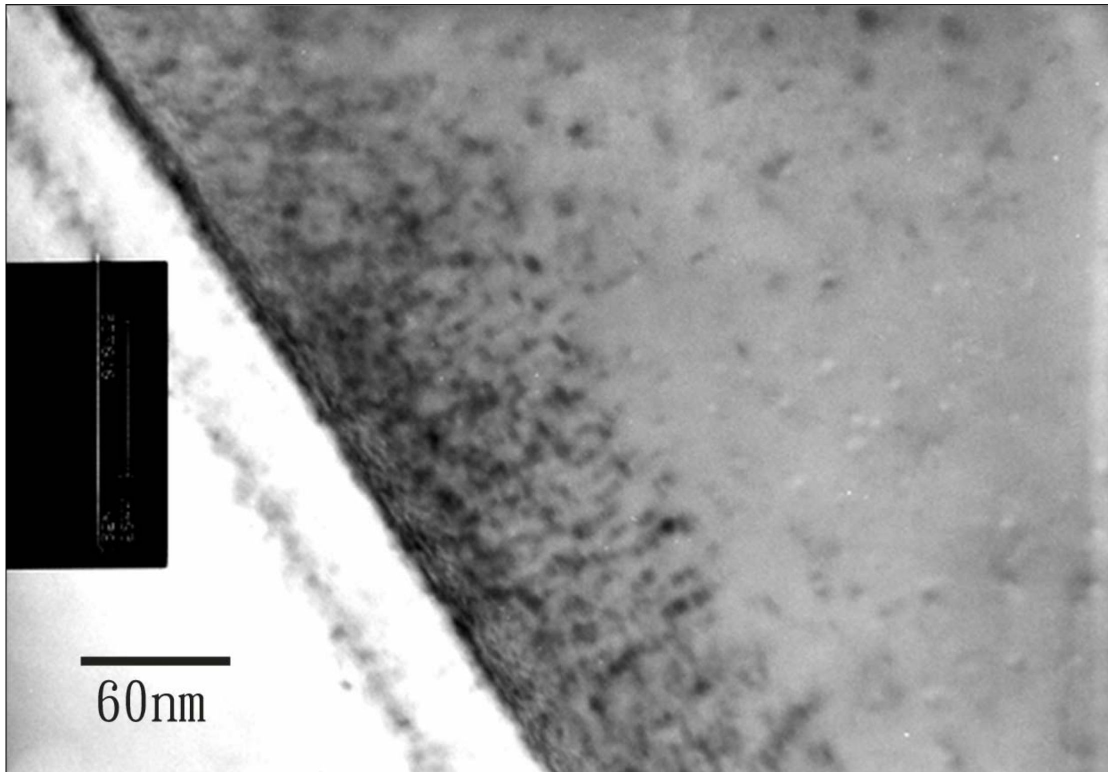

Fig.14 250K BF image of the 300℃ 1hr post-annealed sample

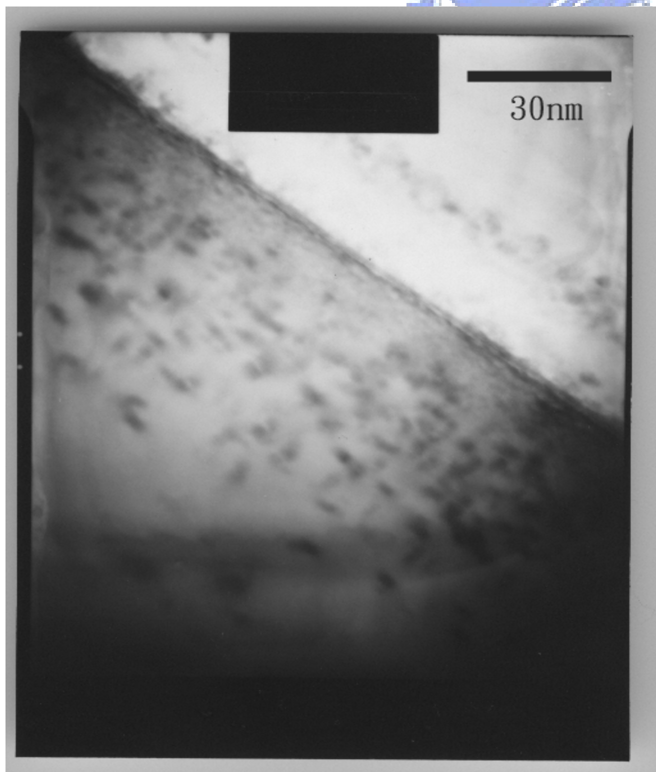

Fig. 15 490K BF image of the 300℃ 1hr post-annealed sample, layer-by-layer interface transition

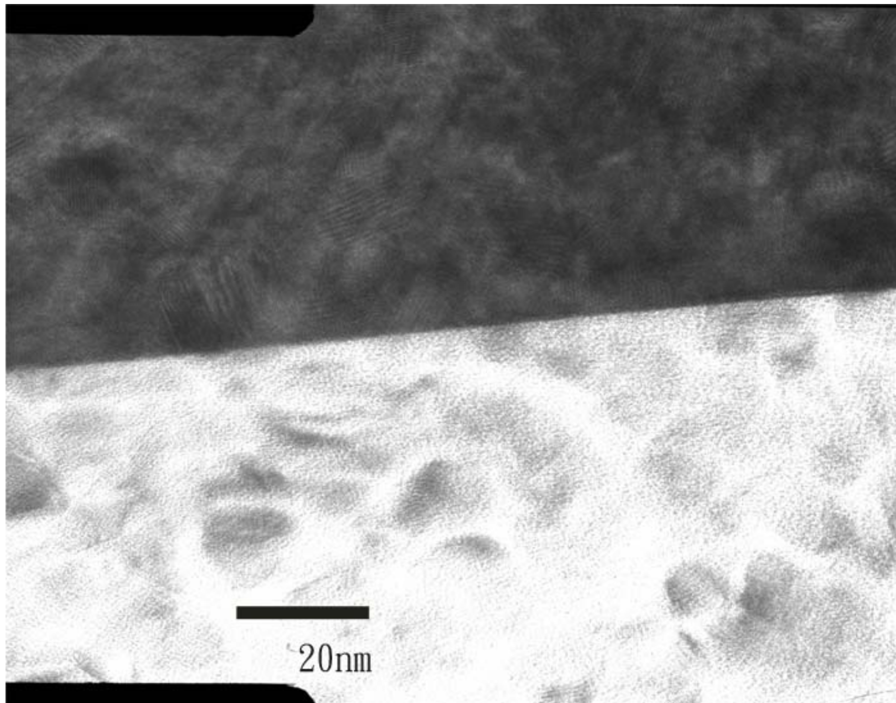

Fig.16 600K HRTEM lattice image of the crystalline/polycrystalline GaN interface for 850℃ 1hr post-annealed sample, the interface was atomic smooth

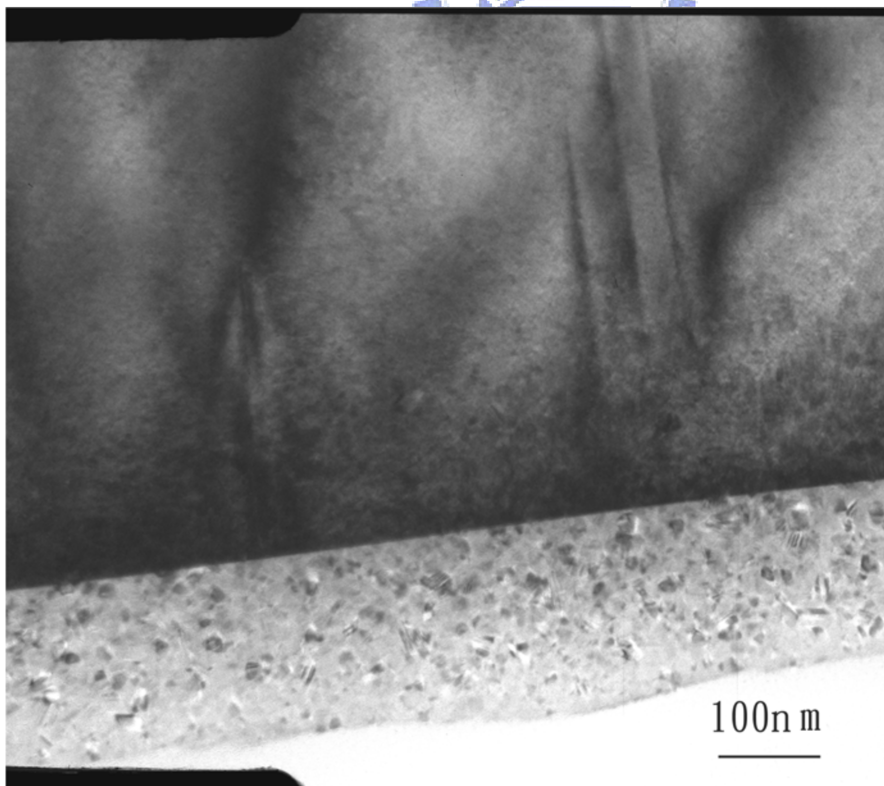

Fig.17 100K BF image of 850℃ 1hr post-annealed sample

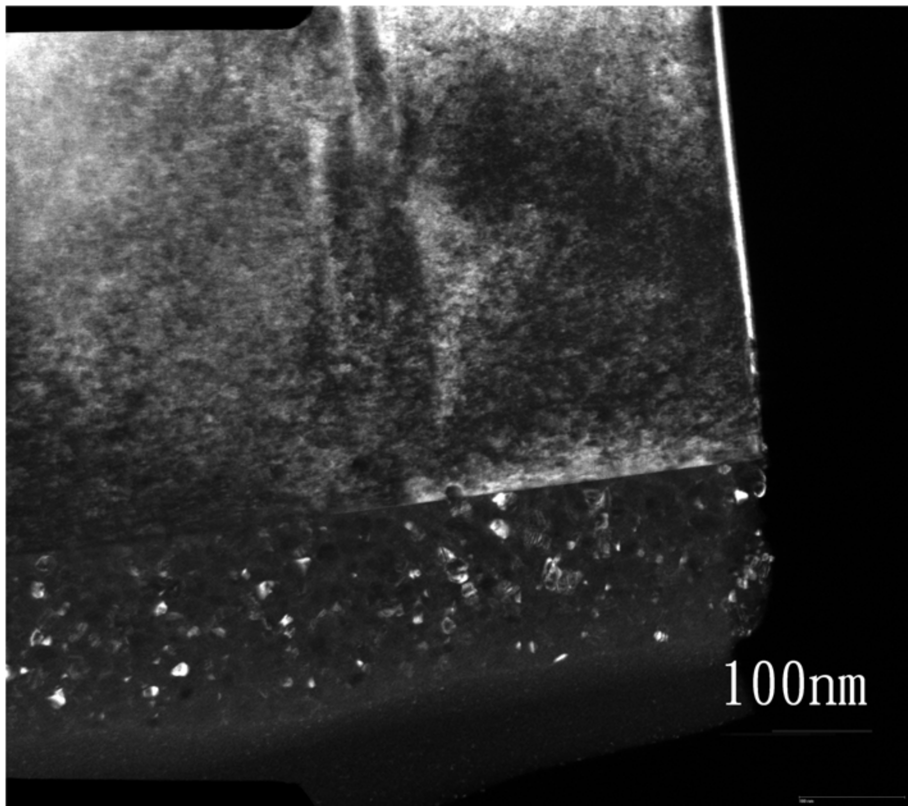

Fig.18 DF the sample of Fig.17

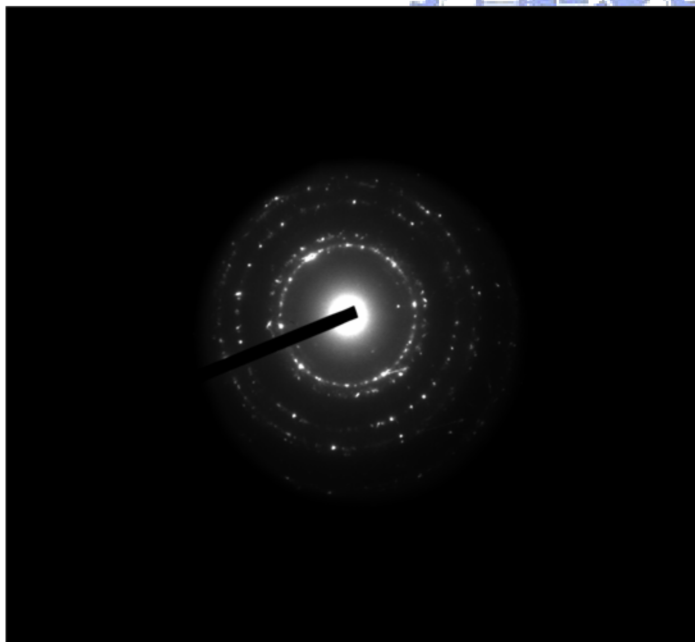

Fig.19 SAD of polycrystalline region in Fig.17

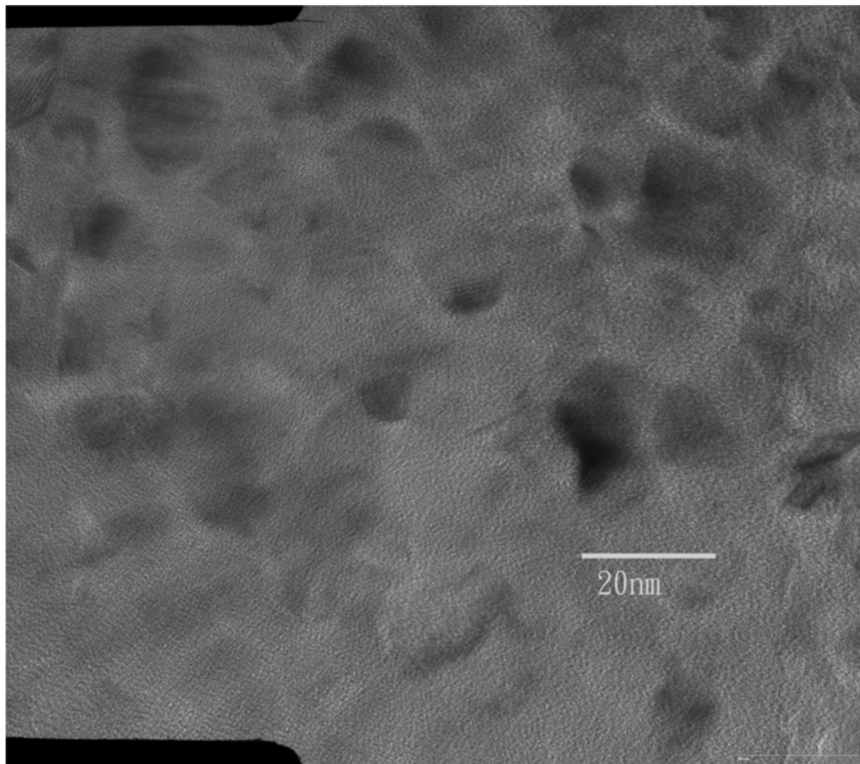

Fig.20 polycrystalline GaN precipitated from the amorphous matrix

600K HRTEM lattice image

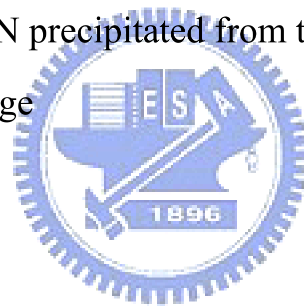

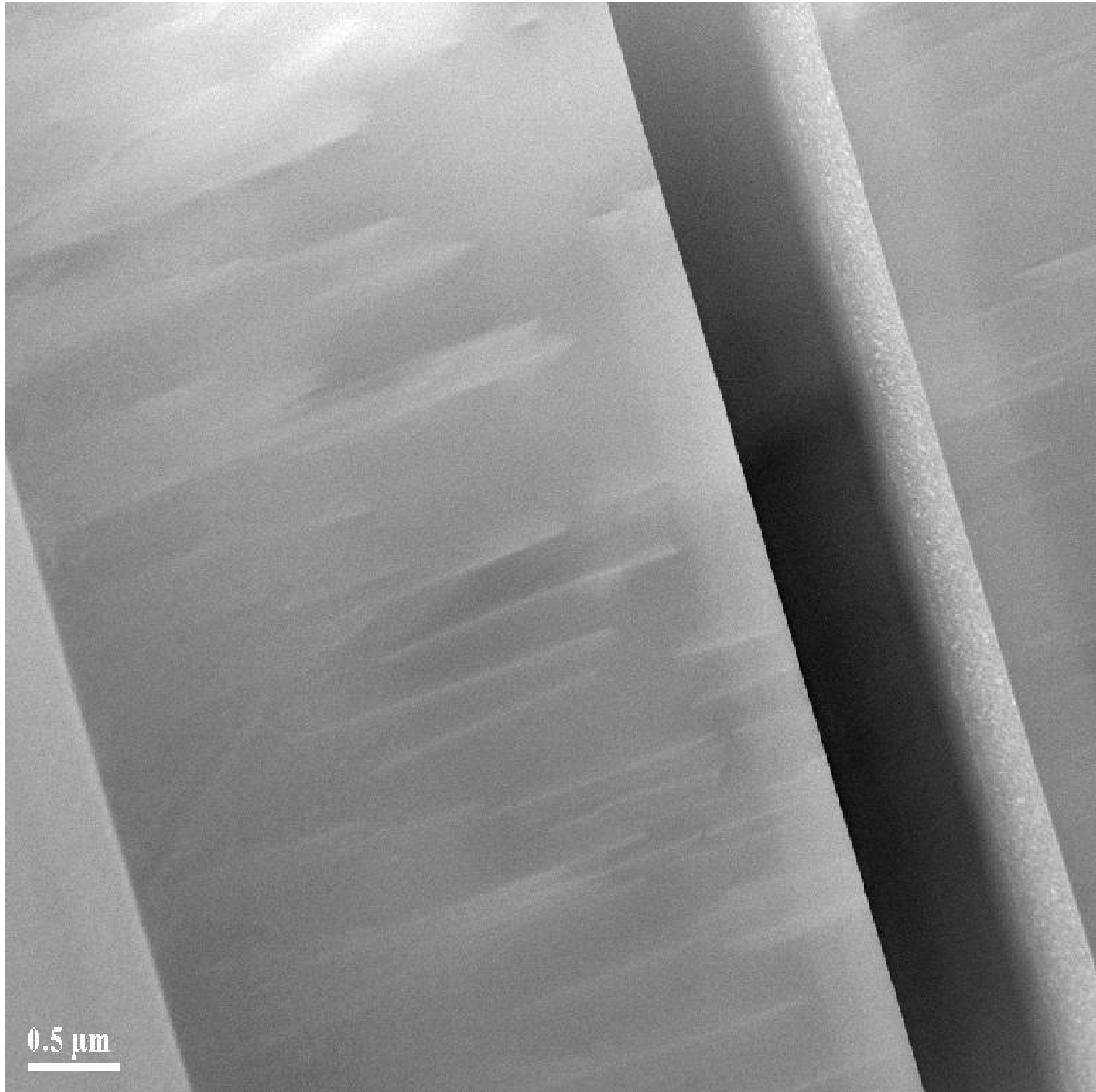

Fig.21 STEM image of the as-implanted (left) and 850°C 1hr post-annealed (right) samples

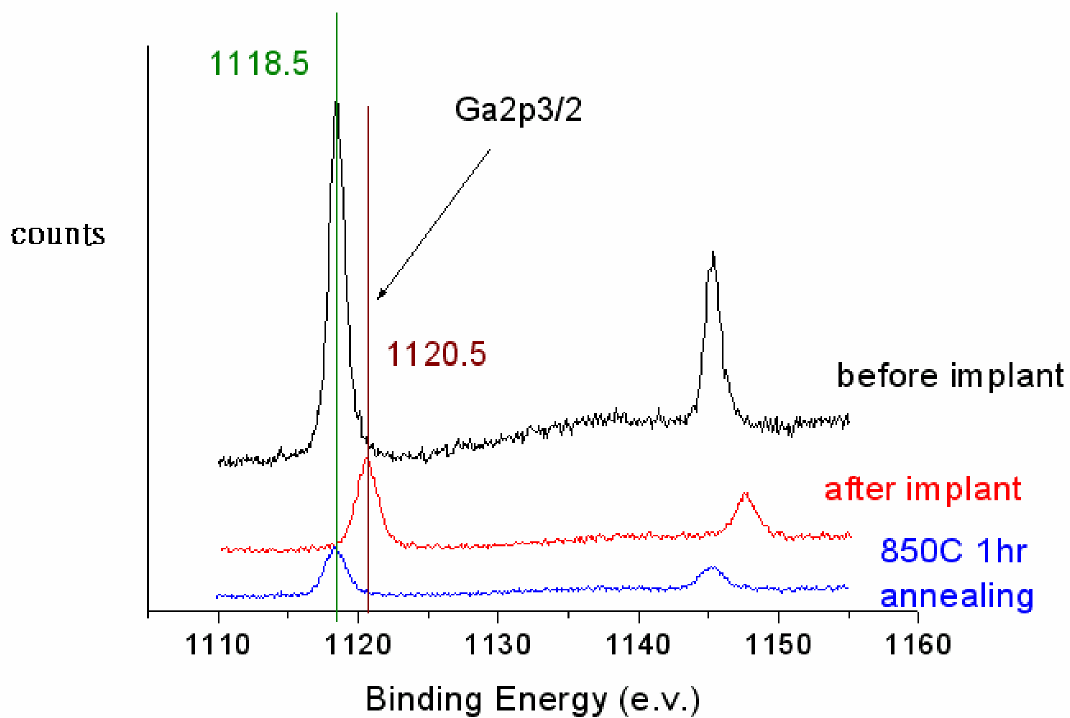

Fig.22 Ga2p$_{3/2}$ binding energy peak at surface region for un-implanted, as-implanted and 850°C 1hr post-annealed samples

Fig.23 600K lattice image of the as-implanted sample

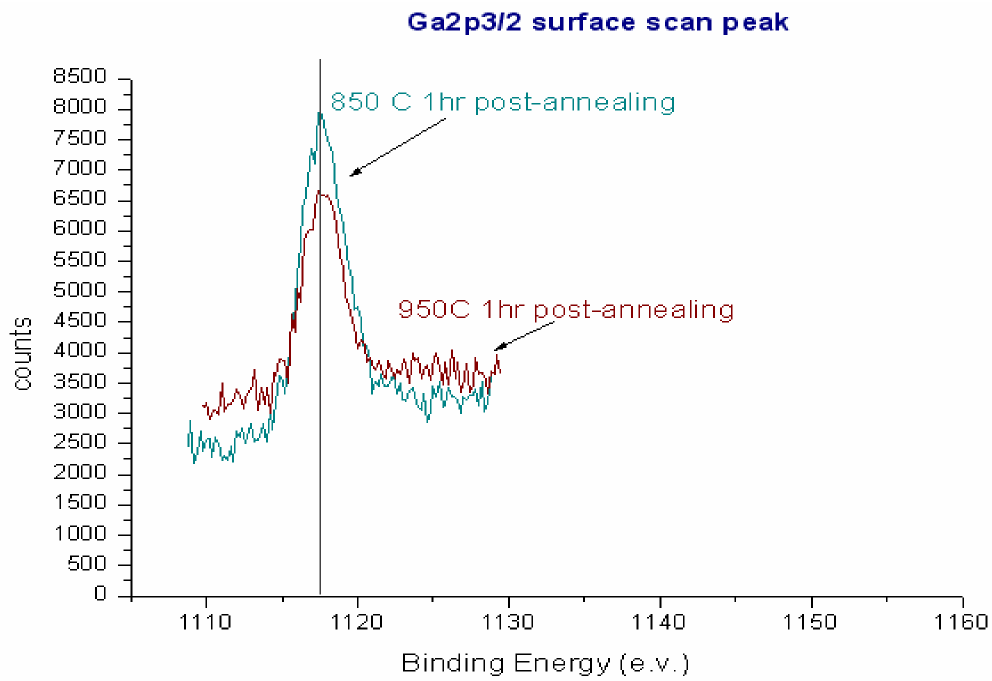

Fig.24 Ga2p$_{3/2}$ binding energy peak at surface region for 850°C and 950°C 1hr post-annealed samples

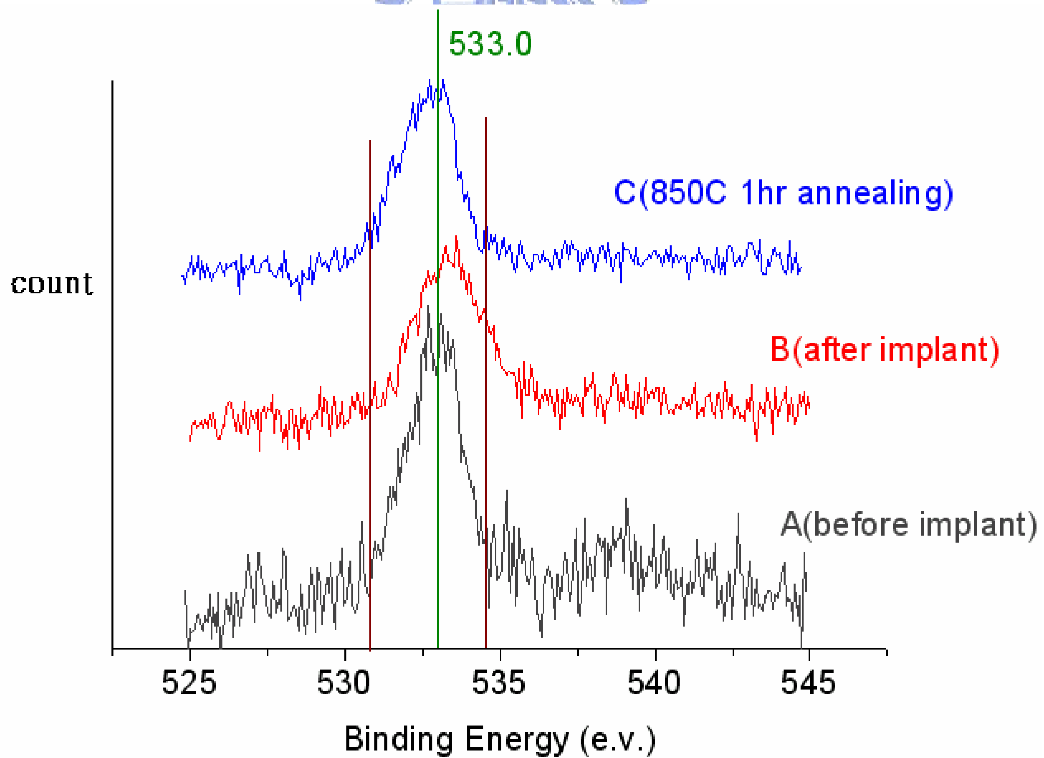

Fig.25 Surface O1s peaks of un-implanted, as-implanted and 850℃ 1hr post-annealed samples

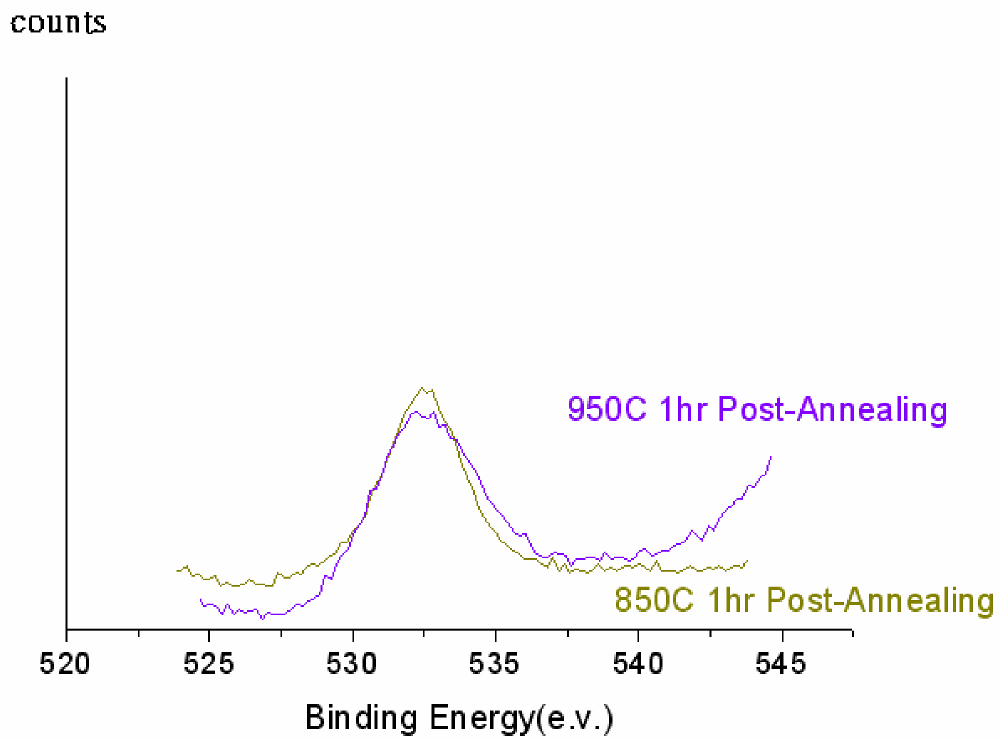

Fig. 26 Surface O1s peaks of the 850℃ and 950℃ post-annealed samples

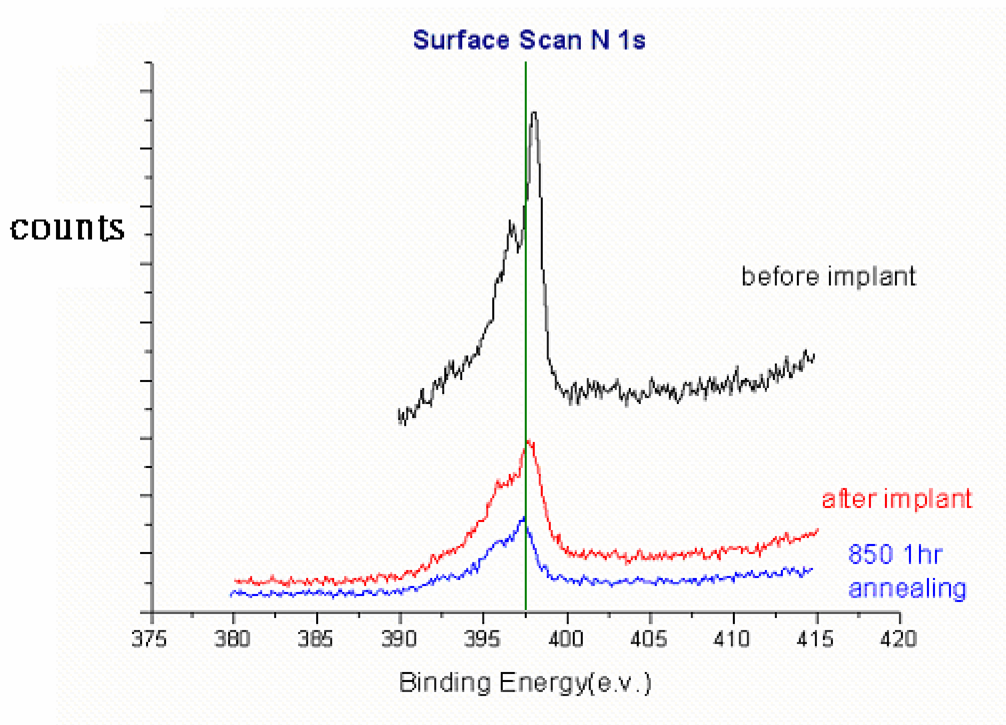

Fig.27 Surface N1s peaks for the un-implanted, as implanted and 850℃ 1hr post-annealed samples

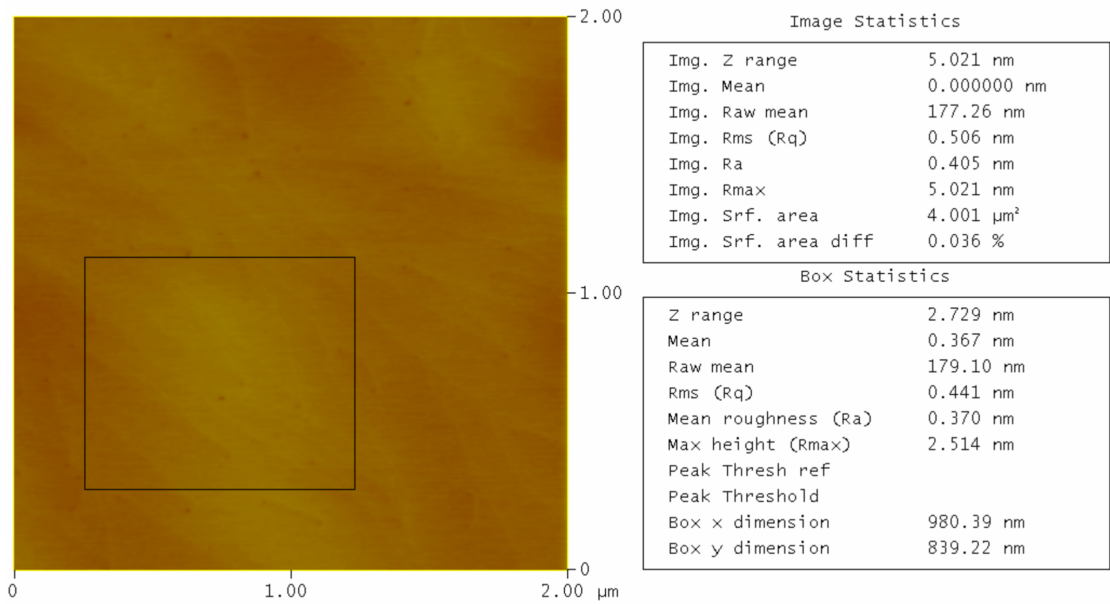

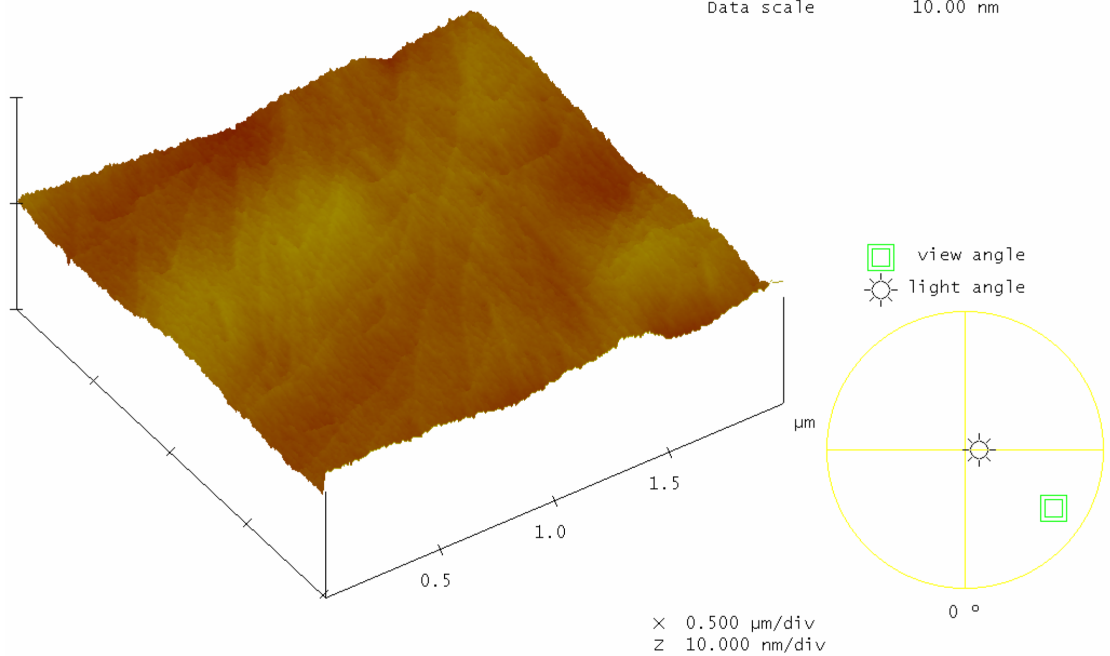

Fig.28 AFM measurement before implantation, R_{rms}=0.506nm

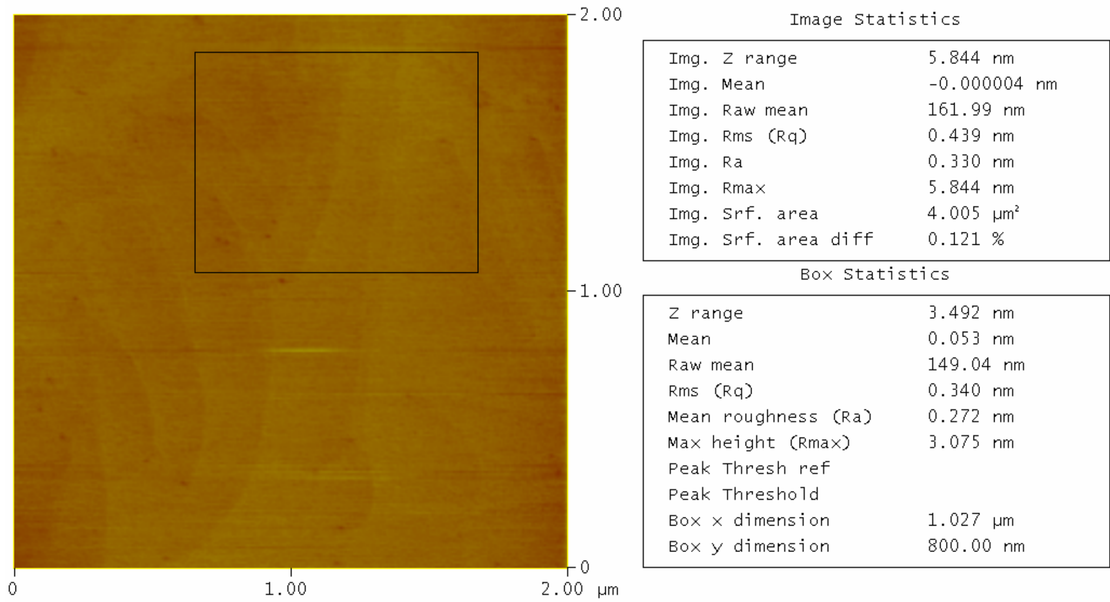

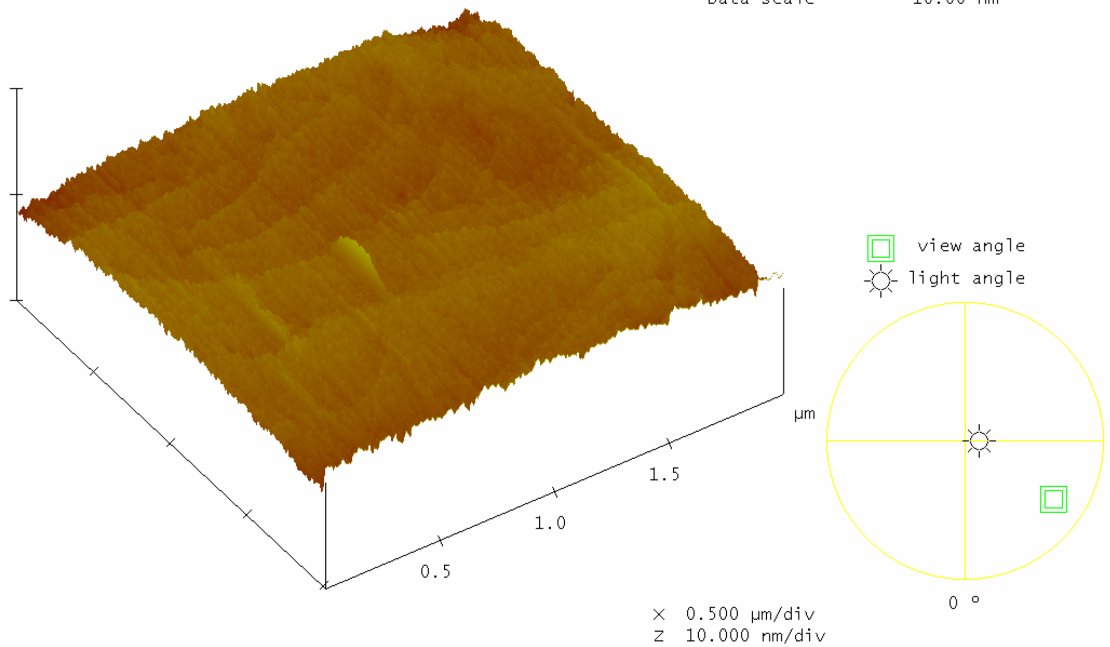

Fig.29 AFM measurement after implantation, R_{rms}=0.34nm

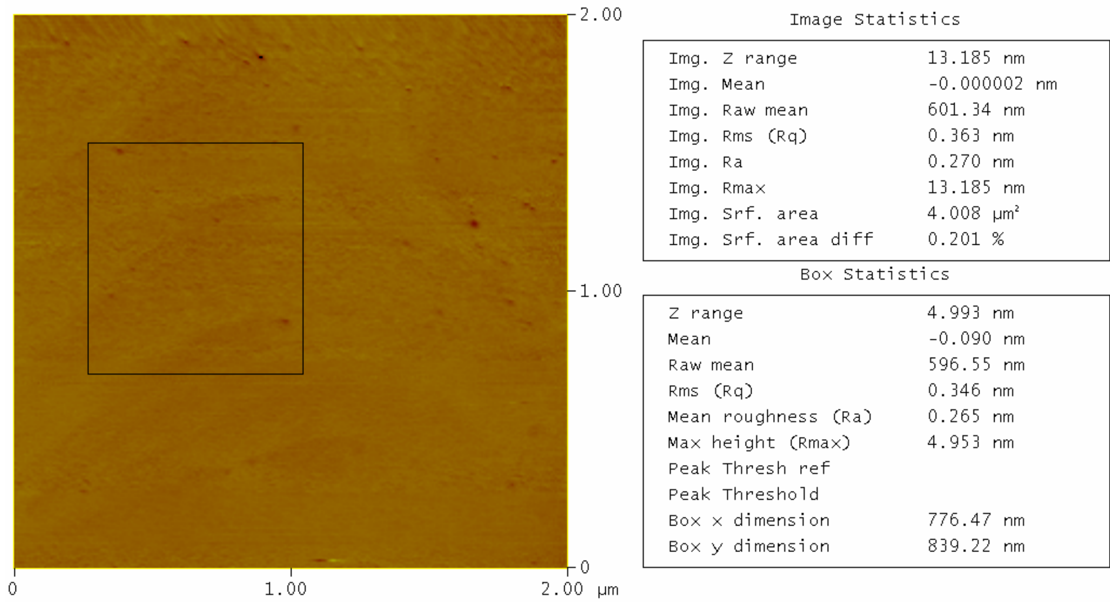

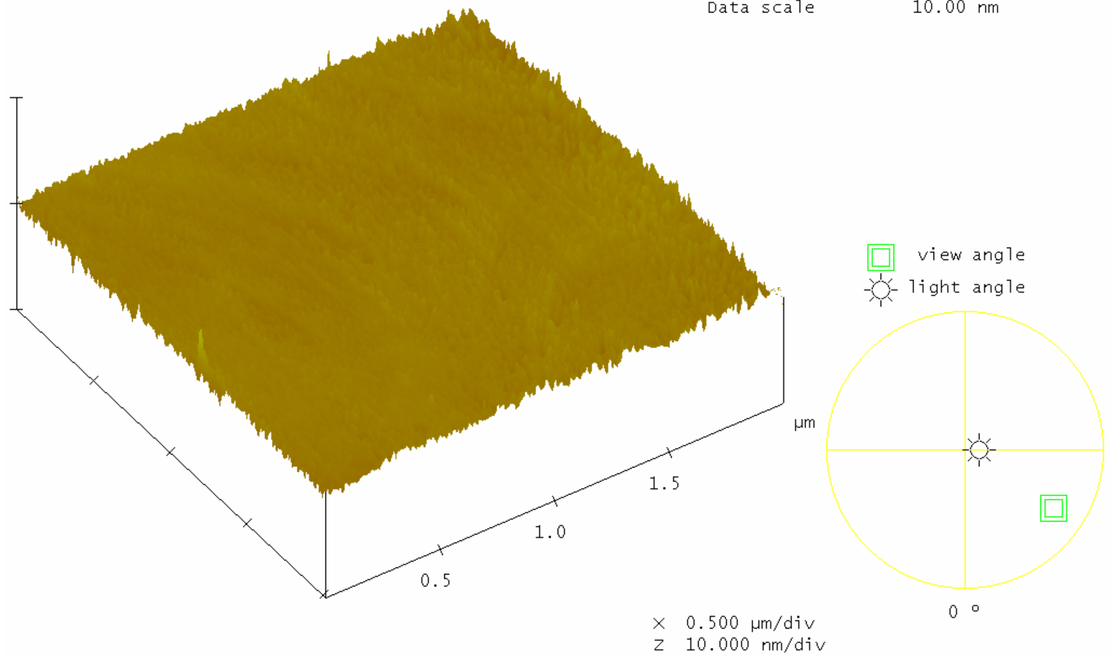

Fig.30 AFM measurements of 950°C 1hr post-annealed sample, R_{rms}=0.346nm

Chapter 5

CONCLUSION

GaN based electronic devices are receiving more and more attention recently for its high power performances and the GaN based power HFET are becoming an uprising industry. Owing to the material characteristics of the GaN itself, damage free etching for mesa isolation of GaN devices was very difficult. Ion implantation isolation provides a new solution for the device isolation. In our study, we tested multi-energy oxygen ion implantation isolation on AlGaN/GaN HEMTs device fabrication. A high saturation current of 673.5mA/mm and a high peak transconductance of 288mS/mm were observed with high off-state breakdown of 87V for the device fabricated. The above device performance values were higher than the AlGaN/GaN HEMTs of the same structure but only differed by using ICP dry mesa etch isolation instead of implantation isolation. The current slump behavior was also suppressed by using implantation isolation. Therefore, we suggest that the multi-energy oxygen ion implantation is suitable for high power AlGaN/GaN HEMTs device fabrication since it results in higher breakdown voltage and saturation current than the AlGaN/GaN HEMTs using conventional ICP mesa etch for isolation.

TEM, ESCA and AFM were also applied to the evaluation of the before implant, after implant and different temperature post-annealed samples. For TEM images, implantation induced defects clustered after 300℃ 1hr post-annealing. As a result, hopping conduction was suppressed and isolation quality was improved. Amorphourization

followed by the polycrystallization of GaN were also discovered at post-annealed samples. As a result, leakage currents flew through the grain boundaries and the isolation quality degraded. The crystalline/amorphous or crystalline/polycrystalline interfaces were atomic smooth due to layer-by-layer transition. ESCA measurement exhibited a $Ga2p_{3/2}$ peak shift from 1118.5eV to 1120.5eV after implantation. We suggest that the shift comes from the implantation induced stress field. And the $Ga2p_{3/2}$ peak shifted back to 1118.5eV after 850℃ 1hr post-annealing. We suggest that this phenomenon is because the high temperature post-annealing process released the stress induced by the ion implantation process. AFM results showed that our multi-energy oxygen ion implantation did not cause the change of the surface morphology. The root-mean-square surface roughness was below 1nm before and after ion implantation. Overall, a planar process for device isolation was achieved by using ion implantation technology. By using this process, the fabricated device quality was improved.

References

[1] Yi-Feng Wu “Very-High Power Density AlGaN/GaN HEMTs” IEEE Transactions on electronic devices, Vol.18, No.3, March 2001

[2] J.C. Zolper “Ca and O ion implantation doping of GaN” Appl. Phys. Lett. 68(14), 1 April 1996

[3] S.C. Binari “H,He and N implant isolation of n-type GaN” J. Appl. Phys. 78(5), 1 september 1995

[4] G. Hanington “P/He ion implant isolation technology for AlGaN/GaN HFETs” Electronic Letters 22nd January 1998 Vol.34 No.2

[5] S.O kucheyev “Ion implantation into GaN” Material Science and Engineering, 33(2001) 51-107

[6] B. Pipeleers “Influence of the implantation angle on the generation of defects for Er implanted GaN” Nuclear Instruments and Methods in Physics Research B 206 (2003) 95-98

[7] J.C. Zolper, A.G. Baca and S.A. Chalmers, Appl. Phys. Lett. **62**, 2536 (1993)

[8] S.J. Pearton, M.P. Iannuzzi, C.L. Reynolds, Jr. and L. Peticolas, Appl. Phys. Lett. **52**, 395 (1998)

[9] J.C. Zolper, D.J. Reiger, A.G. Baca, S.J. Pearton, J.W Lee and R.A. Stall, Appl. Phys. Lett. **69**, 538 (1996)

[10] S.O. Kucheyev “Damage build up in GaN under ion bombardment” Physical Review B Volume 62, Number 11 September 2000

[11] Andre Anders “Handbook of Plasma Immersion Ion Implantation

and Deposition

[12] H.H Tan "Annealing of ion implanted gallium nitride" Applied Physics Letters Volume72, Number10 March 1998

[13] S. Matsusanga "Silicon implantation in epitaxial GaN layers: Encapsulant annealing and electrical properties" Journal of Applied Physics March 2004 Volume 95, Number 5

[14] Yow-Jon Lin "X-ray photoelectron spectroscopy study of $(NH_4)2Sx$-treated Mg-doped GaN layers" Applied Physics Letters 2000

[15] T.L. BARR "Recent advances in X-ray photoelectron Spectroscopy Studies of Oxides" J. Vac. Sci 1991

[16] S. Sienz "In-Situ stress measurement during the ion implantation-induced doping of gallium nitride" Thin Solid Films 415 (2002) 1-4